

1 **High-resolution mantle flow models reveal importance**
2 **of plate boundary geometry and slab pull forces on**
3 **generating tectonic plate motions**

4 **Arushi Saxena¹, Juliane Dannberg¹, Rene Gassmüller¹, Menno Fraters², Timo**
5 **Heister³, and Richard Styron⁴**

6 ¹Department of Geological Sciences, University of Florida, Gainesville, FL, USA
7 ²Department of Earth and Planetary Sciences, University of California, Davis, CA, USA
8 ³Mathematical and Statistical Sciences, Clemson University, Clemson, SC, USA
9 ⁴Global Earthquake Model Foundation, Pavia, Italy

10 **Key Points:**

- 11 • We model plate motions in global instantaneous 3-D mantle convection models
12 with different plate boundary geometries
- 13 • Earth's plate boundaries are not uniform and better described by discrete shear
14 zones in the oceans and distributed faults within continents
- 15 • Slab pull within the uppermost mantle (< 300 km depth) contributes about 70%
16 of the total plate driving force

Corresponding author: Arushi Saxena, saxena.arushi@uf1.edu

17 **Abstract**

18 Mantle convection models based on geophysical constraints have provided us with
 19 a basic understanding of the forces driving and resisting plate motions on Earth. How-
 20 ever, existing studies computing the balance of underlying forces are contradicting, and
 21 the impact of plate boundary geometry on surface deformation remains unknown. We
 22 address these issues by developing global instantaneous 3-D mantle convection models
 23 with a heterogeneous density and viscosity distribution and weak plate boundaries pre-
 24 scribed using different geometries. We find that the plate boundary geometry of the Global
 25 Earthquake Model (GEM, Pagani et al., 2018), featuring open plate boundaries with dis-
 26 crete lithospheric-depth weak zones in the oceans and distributed crustal faults within
 27 continents, achieves the best fit to the observed GPS data with a directional correlation
 28 of 95.1% and a global point-wise velocity residual of 1.87 cm/year. A good fit also re-
 29 quires plate boundaries being 3 to 4 orders of magnitude weaker than the surrounding
 30 lithosphere and low asthenospheric viscosities between 5×10^{17} and 5×10^{18} Pa s. Mod-
 31 els without asthenospheric and lower mantle heterogeneities retain on average 30% and
 32 70% of the plate speeds, respectively. Our results show that Earth’s plate boundaries
 33 are not uniform and better described by more discrete plate boundaries within the oceans
 34 and distributed faults within continents. Furthermore, they emphasize the impact of plate
 35 boundary geometry on the direction and speed of plate motions and reaffirm the impor-
 36 tance of slab pull in the uppermost mantle as a major plate driving force.

37 **Plain Language Summary**

38 Plate tectonics can explain several geological and geophysical phenomena on Earth
 39 and is closely coupled to convection in the underlying mantle. To understand this plate-
 40 mantle coupling and quantify the forces contributing to plate motion, we develop high-
 41 resolution three-dimensional computational models of the Earth’s present-day mantle
 42 flow utilizing available geophysical constraints on density distribution and rheology. Ad-
 43 ditionally, we prescribe weak zones at the location of plate boundaries. We use differ-
 44 ent plate boundary geometries, forming either open or closed polygons, and we vary how
 45 easily the plate boundaries and the asthenosphere directly below the plates can be de-
 46 formed to determine which model best fits observed plate motions. Our best-fitting model
 47 features open plate boundaries that are weak (~ 4 order of magnitude weaker than the
 48 surrounding lithosphere) and traverse the whole plate in the oceans, but are shallower
 49 and more distributed within continents. The asthenosphere in these models is even weaker
 50 than the plate boundaries. Furthermore, we find that the downward force caused by sub-
 51 ducted slabs contributes the most to the observed surface velocities. Our models sug-
 52 gest that plate boundaries are not uniformly weak everywhere and that their geometry
 53 has a strong influence on the direction and speed of plate motion.

54 **1 Introduction**

55 Plate tectonic forces shape some of the most remarkable geological features on Earth
 56 and without plate tectonics, complex life on Earth would not be possible. Therefore, tec-
 57 tonic forces have been studied extensively. With the increased availability of computa-
 58 tional resources and advanced numerical techniques, mantle flow models based on ob-
 59 servational constraints have become an increasingly common tool for investigating global
 60 tectonics and how the contributing plate-driving and resisting forces affect the motion
 61 of plates. These models usually derive their temperature distribution from a seismic to-
 62 mography model, and in some cases additional data sets, and then use the correspond-
 63 ing buoyancy forces to predict global plate motions. For instance, Zhong (2001) stud-
 64 ied the effects of plate-mantle coupling and the viscosity contrast between oceanic and
 65 continental plates on the observed surface plate motions and the geoid, inferring the lo-
 66 cation of subducted slabs from the Earth’s subduction history and using an upper-mantle

67 structure from seismic tomography. To investigate the relative importance of slab pull
 68 and slab suction forces for the plate motions, Conrad and Lithgow-Bertelloni (2002) an-
 69 alyzed a model with slab geometries based on plate reconstructions. Becker (2006) stud-
 70 ied how lateral viscosity variations computed from the SMEAN tomography model (Becker
 71 & Boschi, 2002) affect plate motions and Euler poles. In an advanced high-resolution global
 72 mantle convection model based on tomography and a slab database, Stadler et al. (2010)
 73 resolved plate boundaries at the ~ 1 km-scale to fit the observed plate motions and plate-
 74 ness. Osei Tutu, Sobolev, et al. (2018) investigated the contribution of various plate-driving
 75 and resisting forces on the plate motions and Euler poles using mantle flow models based
 76 on a well-resolved uppermost mantle temperature distribution and the SMEAN tomo-
 77 graphic model at depths >300 km. And Liu and King (2022) explored what drives the
 78 motion of the North American plate by varying the buoyancy forces associated with ve-
 79 locity anomalies in their tomography model.

80 All of these models highlight the importance of buoyancy forces from both the up-
 81 per and the lower mantle for reproducing the observed surface deformation. However,
 82 there are substantial discrepancies between different studies regarding the relative con-
 83 tributions of the forces that drive plate motions. Conrad and Lithgow-Bertelloni (2002,
 84 2004) find that slab pull in the upper mantle accounts for about 50% to 70% of the to-
 85 tal plate driving force and the rest is accommodated by slab suction in the lower man-
 86 tle, emphasizing the importance of upper mantle buoyancy. The models by Stadler et
 87 al. (2010) and Alisic et al. (2012) even show a better fit to the plate velocities if only slab
 88 pull in the upper mantle is considered and the lower mantle is assumed to be homoge-
 89 neous compared models with lower-mantle heterogeneity. On the other hand, the mod-
 90 els of Osei Tutu, Sobolev, et al. (2018) predict that 70% of the plate-driving force comes
 91 from lower mantle buoyancy alone.

92 This difference in model results also highlights that developing self-consistent global
 93 mantle flow models that reproduce the observed plate motions remains a challenging prob-
 94 lem. The complexity of the problem arises from the interplay of numerous physical pro-
 95 cesses governing mantle flow at different time and length scales, and the associated ne-
 96 cessity to incorporate physical properties of vastly different magnitudes from the Earth’s
 97 surface to the core-mantle boundary into a single model (e.g., Schubert et al., 2001; Heis-
 98 ter et al., 2017). The different scale of deformation at plate boundaries compared to con-
 99 vection cells in the mantle means that coupling these processes requires a high resolu-
 100 tion and/or the use of an adaptive grid. This is associated with large computational costs.
 101 Non-linear rheologies and strong viscosity contrasts between plates and plate boundaries
 102 pose challenges for solving the governing equations numerically. Furthermore, the un-
 103 known present thermal and chemical state of the Earth imposes a limit on how well buoy-
 104 ancy forces can be constrained. To achieve the most accurate results, different types of
 105 models and observations (seismic tomography, heat flux, plate age, present and past lo-
 106 cations of subduction zones, plate boundary geometry, etc.) need to be combined. Due
 107 to these challenges, the influence of various model components and the associated phys-
 108 ical properties of the mantle on the observed surface deformation are still open questions,
 109 that we try to answer here.

110 The seismic tomography used as an input determines how well a model can resolve
 111 mantle buoyancy and therefore affects the modeled force balance controlling plate mo-
 112 tions (Becker & O’Connell, 2001). A common choice in previous mantle convection mod-
 113 els has been a degree-20 (S20RTS, Ritsema & Van Heijst, 2000) or degree-40 (S40RTS,
 114 Ritsema et al., 2011) shear-wave velocity model—used by Stadler et al. (2010); Liu and
 115 King (2022), or an averaged shear wave model, SMEAN (Becker & Boschi, 2002)—used
 116 in Becker (2006); Osei Tutu, Steinberger, et al. (2018). Since then, increased station cov-
 117 erage and advances in computational resources have made it possible to create tomog-
 118 raphy models that utilize both P-waves—that can better resolve the subducted slabs (e.g.,
 119 Li et al., 2008; Simmons et al., 2012), and shear-waves—that can better resolve the low-

120 velocity anomalies (e.g., Becker & Boschi, 2002). These more robust models can reach
 121 a resolution of 1 degree (Simmons et al., 2015, 2019), but their effect on the accuracy
 122 of the equivalent buoyant forces and the corresponding plate motions remain to be tested.

123 In order to generate plate-like motion, existing models use weak zones at locations
 124 corresponding to the Nuvel plate boundary model (DeMets et al., 1990). Since then, an
 125 updated plate boundary model by Bird (2003)—comprising of several micro-plates and
 126 regions of more complex deformation inside the plate boundary polygons—has been pro-
 127 posed. Additionally, in an effort to map the global seismic hazard, the Global Earthquake
 128 Model, consisting of over 13,000 active faults and their detailed geometry, has been made
 129 publicly available (Styron & Pagani, 2020). To date, global mantle flow models in the
 130 literature (e.g., Stadler et al., 2010; Osei Tutu, Steinberger, et al., 2018; Liu & King, 2022)
 131 have not studied the effects of different plate boundary geometries (other than Nuvel)
 132 on surface deformation and it remains unclear which plate boundary model best repro-
 133 duces the observed plate motions.

134 Here, we address the questions raised above by developing global compressible man-
 135 tle flow models based on a high-resolution seismic tomography that jointly inverts for
 136 P- and S-wave traveltimes, LLNL-G3D-JPS (Simmons et al., 2015), and four different
 137 plate boundary geometries. We investigate which of the components of a geodynamic
 138 model—and which corresponding force in the Earth’s mantle—is most important to re-
 139 produce the Earth’s present-day plate motions. In addition, we explore how different plate
 140 boundary geometry models affect the surface plate motions and their fit to observations.
 141 Based on the best-fitting model, we quantify the relative influence of the driving and re-
 142 sisting forces on the motion of the tectonic plates.

143 2 Methods

144 2.1 Governing equations

145 We use global 3D instantaneous models of mantle convection, solving the compress-
 146 ible Stokes equations in the following form:

$$-\nabla \cdot (2\eta\dot{\boldsymbol{\varepsilon}}) + \nabla p = \rho\mathbf{g}, \quad (1)$$

$$\nabla \cdot (\rho\mathbf{u}) = 0, \quad (2)$$

147 where η is the shear viscosity, $\dot{\boldsymbol{\varepsilon}}$ is the deviatoric strain rate, p is the pressure, ρ
 148 is the density, \mathbf{g} is the gravitational acceleration, and \mathbf{u} is the velocity. Since our mod-
 149 els are instantaneous, we do not solve equations for the conservation of energy or the
 150 tracking of materials. Therefore, the only material properties directly appearing in the
 151 equations are the density and viscosity. The density depends on pressure, temperature
 152 and composition (Section 2.4), and the viscosity depends on temperature, composition,
 153 depth, and strain-rate (Section 2.5). We note that we use the Anelastic Liquid Approx-
 154 imation (Jarvis & Mckenzie, 1980) to solve equation (2) so it is reformulated to:

$$\nabla \cdot (\rho_{\text{ref}}\mathbf{u}) = 0, \quad (3)$$

155 where $\rho_{\text{ref}}(z)$ is the depth-dependent reference profile. This is an improvement on pre-
 156 vious studies (Osei Tutu, Steinberger, et al., 2018; Liu & King, 2022) that have assumed
 157 an incompressible mantle. To compute the reference profile, we use the density at the
 158 adiabatic pressure and temperature in the uppermost mantle (where temperatures are
 159 based on the TM1 model, see Section 2.3), and PREM below that.

160 Our model geometry is a three-dimensional spherical shell with an inner radius of
 161 3481 km and an outer radius of 6371 km (and accordingly, a thickness of 2890 km). We

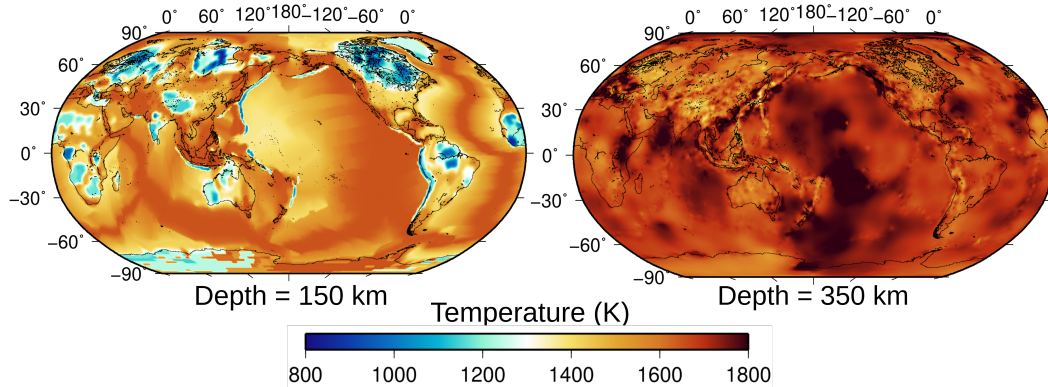


Figure 1. Temperature distribution at depth layers of 150 km (left) and 350 km (right) using the TM1 model (Osei Tutu, Sobolev, et al., 2018) and the LLNL-G3D-JPS tomography model (Simmons et al., 2015), respectively.

162 use free slip boundary conditions at both the top and bottom boundary, and remove the
 163 net rotation of the surface to constrain the resulting rotational degree of freedom. This
 164 allows us to compare modeled surface velocities to measured GPS velocities in a no-net-
 165 rotation reference frame.

166 2.2 Numerical methods

167 To solve Equations (1) and (2), we use the open-source geodynamic modeling soft-
 168 ware ASPECT (Kronbichler et al., 2012; Heister et al., 2017; Bangerth et al., 2022b),
 169 which has been successfully benchmarked for global spherical mantle flow computations
 170 (Liu & King, 2019). ASPECT is a finite-element modeling package that uses stable Taylor-
 171 Hood (Q2Q1) elements to discretize the Stokes system (velocity and pressure), and em-
 172 ploys an iterative preconditioned GMRES solver to solve the resulting linear system.

173 For the Stoke system, we make use of the recently implemented matrix-free solver
 174 and geometric multigrid preconditioner (Clevenger & Heister, 2021), which scales effi-
 175 ciently up to 100,000 compute cores, and reduces ASPECT’s memory requirements sig-
 176 nificantly. This allows us to run large-scale instantaneous models like the ones in this
 177 study on relatively few cores. A requirement of this solver is to cell-wise average the vis-
 178 cosity as defined in Section 2.5, and for our models we choose a harmonic average.

179 ASPECT makes use of the libraries deal.II (Arndt et al., 2021) and p4est (Burstedde
 180 et al., 2011) to discretize the geometry into 3D hexahedra that are organized into a hi-
 181 erarchical unstructured adaptive mesh stored as a forest of octrees. Each hexahedron uti-
 182 lizes a nonlinear fourth-order mapping from unit cell to real cell, which allows to account
 183 for the spherical curvature of each element. To be able to model thin plate boundaries,
 184 we utilize ASPECT’s adaptive mesh and use a resolution between approximately 17 km
 185 and 82 km depending on the location in the model (see Figure 2, right panel). This range
 186 of resolutions results in models of approximately one billion degrees of freedom, with a
 187 typical graphical output size of 18 GB. Our models were run on 5376 cores at the NSF
 188 supercomputing system Frontera at TACC with smaller test models run on 512 cores at
 189 SDSC Expanse.

2.3 Initial temperature and composition

We infer the initial temperature in our model from published crust, lithosphere and subducted slab models (above 200 km depth) and global seismic tomography models (below 200 km depth). Figure 1 shows two depth slices of these two temperature models. In addition, the temperature is fixed to 273 K at the surface and to 3700 K at the core-mantle boundary.

In the top 200 km, we use the temperature distribution of the TM1 temperature model from Osei Tutu, Steinberger, et al. (2018). This model includes the thermal structure of continents based on their age from model TC1 (Artemieva, 2006), temperatures of oceanic plates computed using a half-space cooling model and plate ages from Müller et al. (2008), and vertical slabs using location and depth from Steinberger (2000).

For the rest of the model, we use the joint P- and S-wave 1°-tomography model LLNL-G3D-JPS by Simmons et al. (2015) and use a depth-dependent scaling factor to convert from S-wave velocity anomalies to temperature anomalies (Steinberger & Calderwood, 2006). We add these anomalies to a reference temperature profile based on a mantle adiabat with a potential temperature of 1573 K, which we chose to prevent jumps in the average mantle temperature at 200 km depth between the TM1 and LLNL-G3D-JPS models. To compute the adiabatic profile, we integrate downwards starting from the potential temperature at the surface, using the thermal expansivity profile from Steinberger and Calderwood (2006), a specific heat of 1200 J/kg/K, and the density profile from PREM.

We smooth the transition between the TM1 model above 200 km and the tomography-derived temperature below using a sigmoid function with a half-width of 20 km. This smooth transition avoids jumps in material properties in regions of the model where the temperature deviates from the reference adiabat (in regions where the temperature is equal to the adiabat, our choice of potential temperature guarantees continuity between the two models).

It may be surprising that we compute a temperature field at all, because the instantaneous Stokes equations do not contain the temperature itself. However, the density and viscosity in the Earth’s mantle depend on temperature and composition and therefore we need these fields to compute the material properties in the Stokes equations.

We note that the depth of the transition between a temperature model based on lithosphere thickness and a seismic tomography model is a choice with potentially significant effects on the model results. Previous mantle convection studies (Conrad & Lithgow-Bertelloni, 2006; Becker, 2006; Osei Tutu, Steinberger, et al., 2018) have achieved good results using a transition depth of 300 km. Our choice of using the higher-resolution TM1 model only up to 200 km depth is based on several tests with varying transition depths (between 100 km and 300 km depth, see Table S1 for more details). In these models, a transition depth of 200 km achieved the best fit to observed plate velocities, which is likely caused by a particular assumption of the TM1 temperature model. TM1 introduces vertically dipping cold temperature anomalies at subduction zones to represent subducted slabs, while the fast anomalies in the tomography model obviously occur at the observed slab locations (with varying dip angles depending on the individual subduction zone). In other words, TM1 resolves the slab pull force from vertical slabs in the shallow sublithospheric mantle very well, but has the drawback that many slabs are disconnected from the dipping slabs in the tomography model if the model is used down to 300 km depth. Our chosen transition depth of 200 km is deep enough to accurately reflect the thickness of all oceanic and nearly all continental plates, since cold cratonic roots are represented in the seismic tomography model as well, and at the same time achieves a better connectivity of subducted slabs than a deeper transition. This model outcome again illustrates the importance of resolving slab pull forces and slab connectivity on global plate velocities (see also Zhong et al., 1998; Conrad et al., 2004).

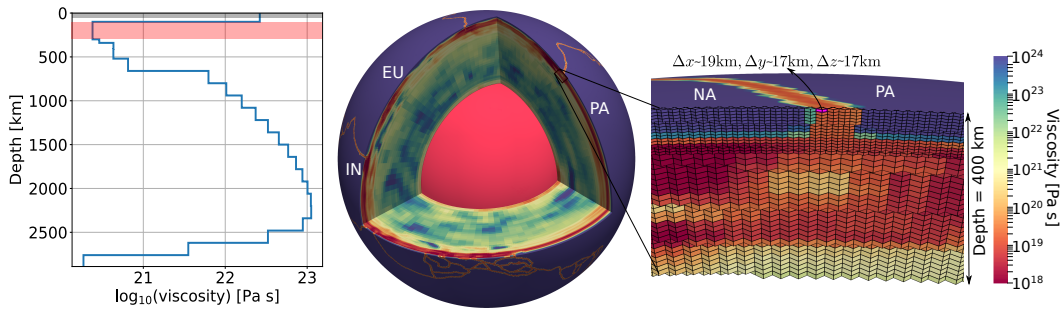


Figure 2. (left) Reference viscosity profile from Steinberger and Calderwood (2006) with a modified low-viscosity asthenosphere extending until 300 km depth (pink layer). (right) Model setup with a cut-out section illustrating the heterogeneous lateral and radial viscosity distribution and a magnified view of the the Aleutian slab showing the mesh geometry adopted in our models. The narrow red zones at the surface represent the imposed plate boundaries where viscosities are several orders of magnitude lower than in the surrounding lithosphere. The abbreviations represent tectonic plates: EU (Eurasian), PA (Pacific), NA (North American) and IN (Indian) plate.

241

2.4 Density distribution

242

243

244

245

246

247

248

249

We base the density in our model on the temperature distribution and seismic velocity anomalies described in the previous section. Above 200 km, we compute the density from the thermal anomalies in the TM1 model relative to a reference temperature of 293 K as done by Osei Tutu, Sobolev, et al. (2018). We use constant thermal expansion coefficients and compressibilities within the crust, lithospheric mantle and asthenosphere (Osei Tutu, Steinberger, et al., 2018), respectively. To define the crust and the lithosphere, we use the lithospheric thickness from Priestley et al. (2018) and crustal thicknesses from the crust1.0 model (Laske et al., 2012).

250

251

252

Below 200 km, we infer the density from seismic tomography. Specifically, we use a depth-dependent scaling factor to convert S-wave velocity anomalies to density (Steinberger & Calderwood, 2006).

253

2.5 Rheology

254

255

256

257

258

259

260

261

262

263

264

265

266

267

268

269

The rheology of our model is purely viscous, temperature- and depth-dependent, and uses an Arrhenius law to describe the different creep mechanisms. We use a combined diffusion/dislocation rheology in the upper mantle and transition zone, and we assume that diffusion creep is dominant in the lower mantle. Prefactors, activation energies and volumes for diffusion and dislocation creep for each major mantle phase are listed in Table 1. To use such a nonlinear viscosity, but simultaneously achieve a viscosity profile that is consistent with constraints from mineral physics and surface observations, we additionally scale the viscosity in each layer of our model so that its lateral average matches the preferred profile of Steinberger and Calderwood (2006) as shown in the left panel of Figure 2. In order to generate a rigid lithosphere, we do not scale viscosities above 60 km depth (gray layer in the left panel of Figure 2). Furthermore, we globally limit the viscosity to make solving the resulting linear system easier. The lower bound is 10¹⁸ Pa s or the prescribed asthenosphere or fault viscosity, whichever value is lower. The upper bound is 10²⁴ Pa s. An example of the resulting viscosity variations is shown in Figure 2 (center). Since the viscosity scaling to the reference profile affects the stresses and strain rates in the model, which in turn influence the dislocation creep viscosity, the combined

Table 1. Flow law parameters used for viscosity

| Parameter | Olivine | Wadsleyite | Ringwoodite | Lower Mantle |
|--|------------------------|------------------------|------------------------|-----------------------|
| Diffusion activation energy, E_{diff} (J/mol) | 370×10^3 | 231×10^3 | 270×10^3 | 299×10^3 |
| Diffusion activation volume, V_{diff} (m^3/mol) | 6×10^{-6} | 6×10^{-6} | 6×10^{-6} | 6×10^{-6} |
| Diffusion creep stress exponent, n_{diff} | 1 | 1 | 1 | 1 |
| Diffusion creep grain size exponent, m_{diff} | 3 | 3 | 3 | 3 |
| Diffusion creep prefactor, A_{diff} $\text{Pa}^{-1}\text{s}^{-1}$ | 1.25×10^{-15} | 6.12×10^{-19} | 2.94×10^{-17} | 5.4×10^{-22} |
| Grain size, d (m) | 5×10^{-3} | 5×10^{-3} | 5×10^{-3} | 5×10^{-3} |
| Dislocation activation energy, E_{disc} (J/mol) | 530×10^3 | 530×10^3 | 530×10^3 | 530×10^3 |
| Dislocation activation volume, V_{disc} (m^3/mol) | 1.4×10^{-5} | 1.7×10^{-5} | 1.7×10^{-5} | 0 |
| Dislocation creep stress exponent, n_{disc} | 3.5 | 3.5 | 3.5 | 3.5 |
| Dislocation creep prefactor, A_{disc} $\text{Pa}^{-1}\text{s}^{-1}$ | 8.33×10^{-15} | 2.05×10^{-12} | 2.05×10^{-19} | 1×10^{-40} |

270 rheology is nonlinear, and requires an iterative solution scheme. We use a fixed-point it-
 271 eration scheme with a nonlinear solver tolerance of 10^{-4} when solving equations (1) and
 272 (2).

273 To facilitate plate-like deformation in our models, we prescribe plate boundaries
 274 as narrow weak zones of reduced viscosity (Figure 2, right panel), taking their locations
 275 from global plate models and fault databases (see Section 2.6.1). We import these plate
 276 boundaries into ASPECT using Worldbuilder (Fraters et al., 2019; Fraters, 2021), an open
 277 source software that facilitates the setup of complex geometries in geodynamic models.
 278 We test 4 different input plate boundary models to investigate the effect of the exact plate
 279 geometry on plate velocities and deformation patterns. Within the weak zones we fix the
 280 viscosity to a constant value that is 3 to 6 orders of magnitude lower than in the sur-
 281 rounding lithosphere (see Table 2 and Section 3.1). This weakening is applied over a width
 282 of 50 km, with the prescribed fault traces at the center. Around this weak zone, the vis-
 283 cosity transitions to the value of the surrounding lithosphere following a hyperbolic tan-
 284 gent along each side of the fault.

285 We note that in reality, brittle failure would create essentially discrete faults in the
 286 crust, and even lithospheric shear zones are generally much thinner than the weak zones
 287 in our models. Our premise here is that a weak zone of a finite width with an appropri-
 288 ately chosen viscosity can approximate the behavior of more complex rheologies suffi-
 289 ciently well to allow accurate plate motion models on continental and global scales. Our
 290 approach contains a trade-off between the thickness and the viscosity of a weak zone.
 291 For a given driving force, the same relative velocities between plates can be obtained in
 292 a model with a thinner and lower-viscosity weak zone on the one hand, or a thicker less-
 293 weak zone on the other hand. We have chosen a shear zone thickness that is appropri-
 294 ately resolved by several mesh cells in our standard resolution, which at the same time
 295 ensures we adequately resolve deformation around and inside the weak zone, and makes
 296 solving the equations computationally simpler. However, this means that the optimal
 297 viscosity in the weak zones in our models is not indicative of the actual viscosity in plate
 298 boundary zones on Earth, which display much more complex deformation processes.

299 2.6 Set of model configurations

300 In order to constrain the importance of the different model components and the
 301 associated plate driving and resisting forces, we vary the following model parameters:

- 302 1. the geometry of the plates and plate boundaries,
- 303 2. the prescribed viscosity of the plate boundaries (controls friction between plates),
- 304 3. the reference viscosity of the asthenosphere (controls the friction at the base of
- 305 the plate),
- 306 4. the strength of cratons (also controls the friction at the base of the plate),
- 307 5. the temperature distribution in the model (controls slab pull forces), and
- 308 6. the viscosity of subducted slabs (controls how well negative buoyancy forces from
- 309 slabs are transferred to the plates).

310 We describe each of these parameters in detail below. A summary of the varied param-
 311 eters is given in Table 2.

312 ***2.6.1 Plate boundary geometry***

313 The general location and distribution of global plate boundaries is relatively well
 314 known. However, their individual structure and precise location varies between differ-
 315 ent plate boundary models. Additionally, depending on the source data used to deter-
 316 mine plate boundary locations, they may be closed or open, and they may include only
 317 clearly defined plate boundaries, or additional diffuse fault zones. We take this uncer-
 318 tainty into account by using a number of different fault database models to determine
 319 the locations of weak zones in our models. Previous work has demonstrated that the ge-
 320 ometry and location of weak zones significantly influences the deformation patterns within
 321 a model (Van Wijk, 2005; Balázs et al., 2018), however to our knowledge, such an anal-
 322 ysis has not been done in global mantle flow models. Therefore, it is unclear how a small
 323 change in the geometry of plate boundaries will exactly influence global plate motions,
 324 and what type of plate boundary model will reproduce present-day observations best.
 325 We use four different fault database models to evaluate their effects on the surface plate
 326 motions: Nuvel (DeMets et al., 1990), Bird closed plate boundaries (Bird, 2003) (Bird-
 327 closed), the Global Earthquake Model (Pagani et al., 2018; Styron & Pagani, 2020) (GEM),
 328 and a limited subset of GEM (Bird-GEM) (Fig 3). The Bird-GEM model is derived from
 329 GEM, but uses only the faults at Bird (2003)’s plate boundaries without any intraplate
 330 faults or diffused deformation zones. Specifically, the model includes oceanic boundaries
 331 similar to the plate boundaries defined in the Bird closed plate boundaries model, but
 332 does not include plate boundaries within continental regions (Bird, 2003). Since GEM
 333 represents the locations of high seismic hazard (Pagani et al., 2018) and not rigid plates
 334 with respective Euler poles—as is generally done to describe tectonic plates (DeMets et
 335 al., 1990; Bird, 2003)—the faults in the GEM and Bird-GEM models do not necessar-
 336 ily map into closed polygons (Figure 3), while the boundaries in the Nuvel and Bird-closed
 337 models do. Another difference between the fault models is that both GEM and Bird-GEM
 338 models have dipping faults based on the seismicity distribution used to develop the GEM
 339 model, while we impose vertical plate boundaries in the Nuvel and Bird-closed models.
 340 The plate boundary shear zones in all models extend until the lithospheric depth defined
 341 by Priestley et al. (2018), except in the case of intraplate deformation in the GEM model
 342 where we use the fault depths included in the database.

343 ***2.6.2 Friction between plates and at the base of plates***

344 Global surface velocities are influenced by the plate boundary friction and the fric-
 345 tion at the base of the lithosphere as observed in previous mantle convection models (Alisic
 346 et al., 2012; Osei Tutu, Sobolev, et al., 2018). In particular, the importance of friction
 347 at cratonic roots is illustrated by the fact that plate speed decreases with increasing con-
 348 tinent area (Forsyth & Uyeda, 1975).

349 We set the viscosity within the plate boundaries to a constant value that is three
 350 to six orders of magnitude lower than the value of 10^{24} Pa s in the surrounding litho-

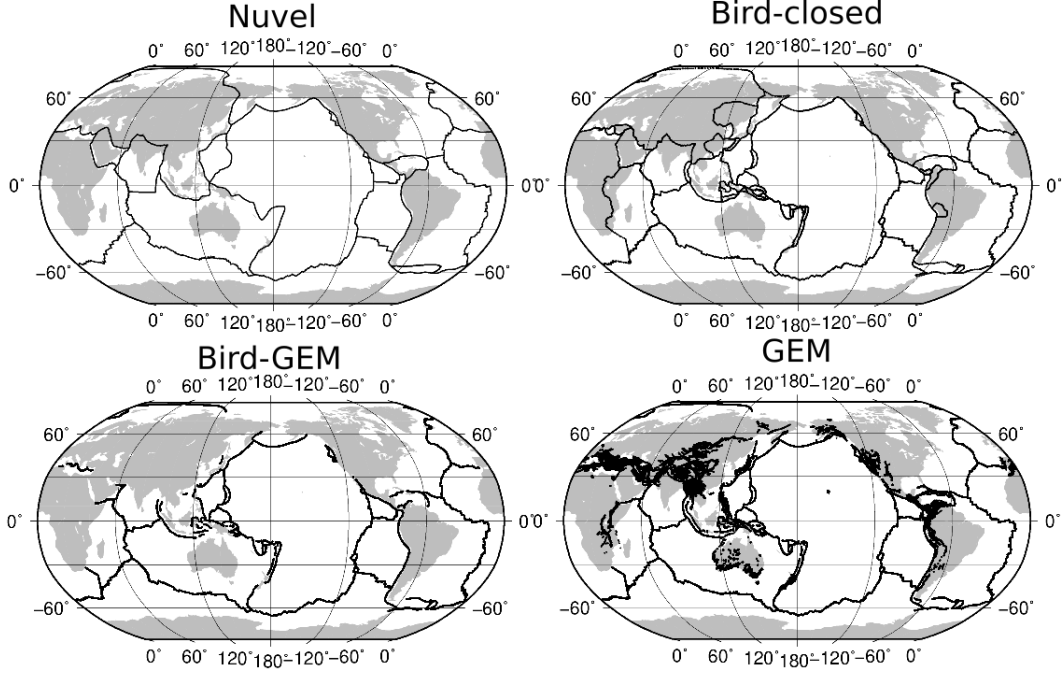


Figure 3. Plate boundary models used in our model setup. See text for details about these models.

Table 2. Parameter values investigated in this study (reference model in bold).

| Plate boundary viscosity (Pa·s) | Asthenosphere viscosity (Pa·s) | Plate boundary model* |
|--|--|-----------------------|
| 10^{21} | 5×10^{19} | Nuvel |
| 5×10^{20} | • 10^{19} | Bird-closed |
| 2.5×10^{20} | • 5×10^{18} | • GEM |
| 10^{20} | • 10^{18} | • Bird-GEM |
| 5×10^{19} | • 5×10^{17} | • |
| 10^{19} | | |
| 10^{18} | | |

*See text for the references to the plate boundary models. Values marked with a • represent runs we selected for all plate boundary configurations after the initial parameter analysis.

351 sphere to allow for plate-like surface motions (Table 2, see also Section 2.5). In addition,
 352 we vary the viscosity of the asthenosphere layer—in our case defined as the sublithospheric
 353 mantle down to 300 km depth, see pink layer in the left panel of Figure 2—in our refer-
 354 ence viscosity profile taken from Steinberger and Calderwood (2006). Specifically, we
 355 reduce the asthenosphere viscosity from the reference value of 2.4×10^{20} Pa s to a range
 356 of values between 5×10^{19} Pa s and 5×10^{17} Pa s (Table 2). Since basal drag is a re-
 357 sisting force in most cases, a low-viscosity asthenosphere implies lower frictional resis-
 358 tance to the motion of the overlying plates and is expected to lead to faster plate speeds.

359

2.6.3 Slab and craton strength

360

361

362

363

364

365

366

367

368

369

370

371

372

373

374

375

376

After determining the most realistic values for asthenospheric viscosity, plate boundary model, and plate boundary viscosity by analyzing the fit to the direction and the speed of plate motions, we also investigate the influence of the strength of cratons and slabs in this best-fit model. The strength of slabs controls the stress partitioning in the lithosphere and thus affects surface plate motions (Billen & Hirth, 2007; Alisic et al., 2010). Therefore, global mantle flow models often introduce highly viscous slabs to better match observed surface velocities (Wu et al., 2008; Alisic et al., 2010). Because we scale the average viscosity in each depth layer of our model to match a reference viscosity profile (Steinberger & Calderwood, 2006), the scaled viscosity of our slabs in the weak asthenosphere is lower compared to the viscosity value that would result purely from the use of our Arrhenius law at low temperatures. To test the impact of stronger slabs, we remove this scaling of the viscosity in the parts of the asthenosphere where non-adiabatic temperatures are below -100 K. This ensures that the slab viscosity is not decreased through re-scaling as the rest of the asthenosphere, allowing us to quantify the effect of the strength of slabs on the plate motions. We note that this algorithm also increases the viscosity in the colder regions below the cratonic lithosphere, since the scaling is not applied to those areas either.

377

378

379

380

381

382

383

384

The strength of cratons impacts the plate–mantle coupling, which can affect plate velocities (Conrad & Lithgow-Bertelloni, 2006; Rolf & Tackley, 2011; Osei Tutu, Sobolev, et al., 2018). Therefore, we investigate the influence of strong cratons in our models, using locations from Nataf and Ricard (1996). In regions defined as cratons, we increase the viscosity within the lithosphere to 10^{25} Pa s, compared to the surrounding lithospheric viscosity of 10^{24} Pa s. Within the cratons, we also set the lithosphere density to our reference adiabatic profile. This makes cratons neutrally buoyant and compensates for compositional density differences within the cratonic lithosphere.

385

2.6.4 Temperature distribution

386

387

388

389

390

391

392

393

394

395

396

397

398

399

400

401

402

In order to quantify the influence of the different sources of buoyancy in our models, we varied the temperature distribution of the model configuration that yielded the best fit to the observed plate motions in the above-mentioned parameter study (asthenosphere viscosity of 5×10^{17} Pa s, GEM plate boundary model (Pagani et al., 2018), and plate boundary viscosity of 2.5×10^{20} Pa s). To quantify the influence of buoyancy forces, specifically slab pull associated with the temperature distribution based on seismic tomography, we ran a model that only includes the temperature variations from TM1 and has an “empty” mantle below 200 km depth. Second, to investigate the effect of slab pull in the upper mantle, we ran a model that only included an adiabatic temperature profile in the sub-lithospheric mantle in the uppermost 200 km—in other words, the only temperature heterogeneities come from lithospheric thickness variations—and the LLNL-G3D-JPS tomography model below. Third, we want to account for uncertainties in lithospheric thickness and further investigate the importance of viscous drag within the uppermost mantle (i.e., 200 km) compared to the underlying convective flow. For this purpose, we run models where we shift the temperatures from the TM1 model in the uppermost mantle by 30 km (both upwards and downwards) to represent a thinner and a thicker lithosphere, respectively (see Supporting Information).

403

2.7 Misfit analysis

404

405

406

To quantify how well our models reproduce the observed plate motions, we compare the modeled surface velocities ($\mathbf{u}^{\text{model}}$) to observed GPS velocities (\mathbf{u}^{obs}) in a net rotation frame (Kreemer & Holt, 2001). We compute three different indicators:

- 407 1. The root-mean-square boundary velocity residual, i.e. $\delta V_{\text{rms}} = \left(\frac{1}{S} \int_S \|\mathbf{u}^{\text{obs}} - \mathbf{u}^{\text{model}}\|^2 dS\right)^{\frac{1}{2}}$,
 408 where $\|\cdot\|$ denotes the L_2 -norm and S the surface area of the model. The RMS
 409 velocity residual provides the most objective measure for the difference between
 410 model and plate velocities. While it cannot distinguish *how* the velocities in the
 411 model differ from observations, it is the best measure to assess the fit between the
 412 models and reality.
- 413 2. The angular correlation-like measure $\xi = \frac{\int_S \|\mathbf{u}^{\text{obs}}\|^2 \hat{\mathbf{u}}^{\text{obs}} \cdot \hat{\mathbf{u}}^{\text{model}} dS}{\int_S \|\mathbf{u}^{\text{obs}}\|^2 dS}$, where $\hat{\mathbf{u}}$
 414 represents the respective normalized unit vectors. ξ allows us to identify how much
 415 of the misfit is caused by the direction of plate motion. This angular mean is weighted
 416 by the square of the observed velocity magnitudes to give more weight to regions
 417 that exhibit stronger flow. This measure is similar to the angular correlation defined by Becker (2006); Liu and King (2022), except that they use the product of
 418 observed and modeled velocity magnitudes as weights whereas we use only the observed
 419 velocities to avoid giving not enough weight to areas where the modeled
 420 velocities are very small. ξ varies between -1 and 1 , where a value of 1 corresponds
 421 to a perfect correlation between observed and modeled plate motion directions.
 422 Our modification of the definition results in overall lower values of ξ for all models.
 423 To be able to compare our results to Becker (2006); Liu and King (2022), we
 424 provide both measures in Section 3.5.3.
- 425 3. The mean speed residual, i.e., $\frac{1}{S} \int_S \|\mathbf{u}^{\text{obs}}\| - \|\mathbf{u}^{\text{model}}\| dS$. The mean speed residual
 426 allows us to identify how much of the misfit is caused by the speed of plate
 427 motion. The misfit in absence of any plate motion would be 3.8 cm/yr, which is
 428 the mean speed of the GPS data. Note that this misfit is computed as integral of
 429 the point-wise difference between the velocity magnitudes. It is not the difference
 430 in the average speed of all plate motion, as done in some other studies.
 431

432 We have implemented the computation of the root-mean-square boundary velocity
 433 residual as a postprocessor in ASPECT so that it is available to the community for
 434 future studies. In addition, we provide scripts to compute the angular correlation and
 435 speed residual as data publication (Saxena et al., 2022).

436 3 Results

437 3.1 Influence of plate boundary weakness and basal drag

438 To obtain a good fit between our dynamic models and the observed plate motions,
 439 we varied the influence of the asthenospheric viscosity (affecting the amount of basal drag
 440 on the plates) and the plate boundary viscosity (affecting friction between plates). For
 441 this parameter study, we used the Bird closed plate boundary geometry. Our results (Figure
 442 4) show that both parameters have a strong influence on the speed and the direction
 443 of plate motion. The speed of plates increases both for lower asthenosphere viscosities
 444 and weaker plate boundaries as indicated by the increased velocity residuals for these
 445 values. However, the plate boundary viscosity affects the plate motions considerably more:
 446 The RMS velocity and mean speed residuals (Figure S1) are reduced by an order of magnitude
 447 as the plate boundary viscosity increases from 10^{18} Pa s to 10^{20} Pa s. A further
 448 increase in plate boundary viscosity to 10^{21} Pa s slightly increases these residuals again
 449 for all chosen values of asthenospheric viscosity. On the other hand, the fit to the direction
 450 of plate motion generally improves with increasing fault viscosity, and we achieve
 451 the best directional fits of $\xi = 0.87 \dots 0.91$ for fault viscosities of 10^{21} Pa s (see Table
 452 S2). This value is consistent with the results of both Liu and King (2022), whose best-fitting
 453 viscosity model also has a plate boundary viscosity of 10^{21} Pa s, and Ghosh and
 454 Holt (2012), who used a spatially variable viscosity in their plate boundary zones based
 455 on strain rate magnitudes in a global kinematic model and achieved a good fit for vis-

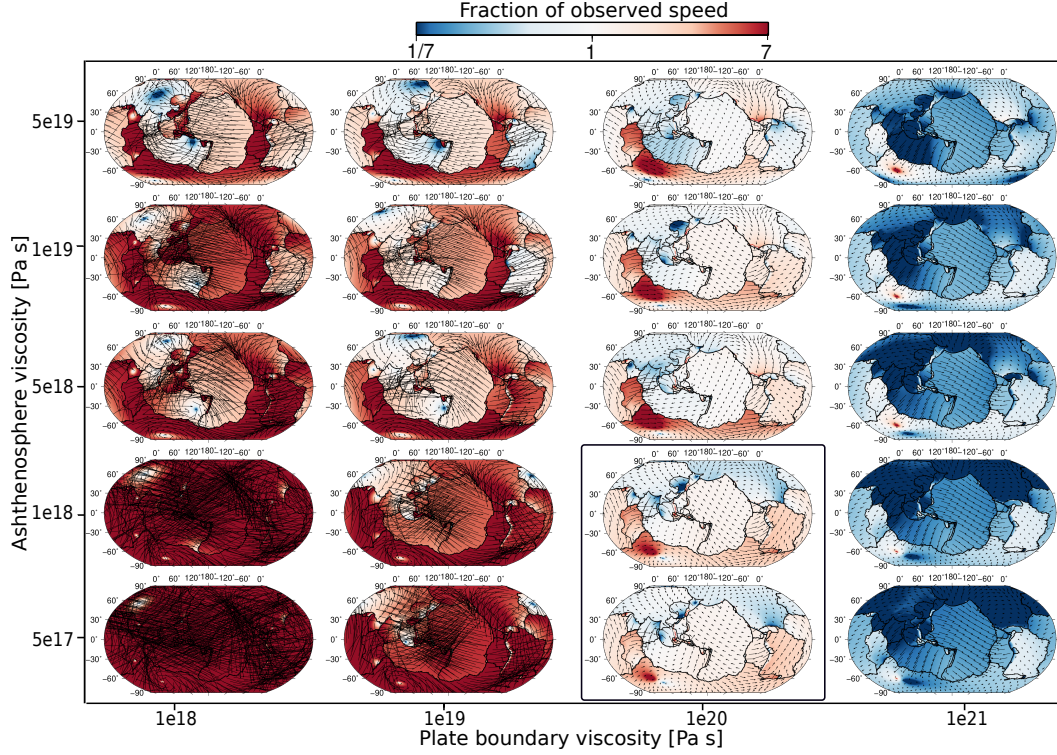


Figure 4. Fraction of modeled speed relative to the observed GPS speeds at the surface for different combinations of plate boundary viscosity and asthenosphere viscosity, and using the Bird-closed plate boundary model (Bird, 2003). The arrows represent point-wise differences between modeled and observed velocity vectors. The black box marks the models with the lowest RMS velocity residual.

456 cosities varying between 10^{20} and 10^{22} Pa s. However, this general trend is very differ-
 457 ent from the results of Osei Tutu, Sobolev, et al. (2018), who include plastic yielding at
 458 plate boundaries and find that increasing the plate boundary friction coefficient also increas-
 459 es the angular misfit, especially for low asthenosphere viscosities. Our models with
 460 the overall best (RMS velocity) fit have intermediate plate boundary viscosities ($\approx 10^{20}$ Pa s)
 461 and low to intermediate asthenosphere viscosities ($\leq 10^{18}$ Pa s).

462 If the plate boundary viscosity is higher than $\approx 10^{20}$ Pa s, all plates are moving
 463 too slowly (Figure 4, right column). Since the high plate boundary strength controls plate
 464 motions, the speed remains almost unchanged for different asthenosphere viscosities.

465 Conversely, if the asthenosphere viscosity is high, but the fault viscosity is low, basal
 466 drag controls the plate motion. In this case, the smallest plates move too fast, especially
 467 the ones directly attached to subducted slabs (Nazca, Arabian, Cocos, Philippine plates),
 468 but also many of the very small plates of the Bird model that are not considered in the
 469 Nuvel model, like Scotia and the smaller plates near Indonesia (Figure 4, top left pan-
 470 els). This can be explained by smaller plates having a higher ratio of plate boundary length
 471 over area. In other words: Smaller plates are controlled more by the friction at their bound-
 472 aries, whereas larger plates are influenced more by the friction at their base. Consequently,
 473 weak plate boundaries allow the small plates to move much faster than they should, whereas
 474 large plates are still limited in their speed. If both viscosities are low, all plates simply
 475 move too fast, and the overall residual is large everywhere (Figure 4, bottom left pan-
 476 els).

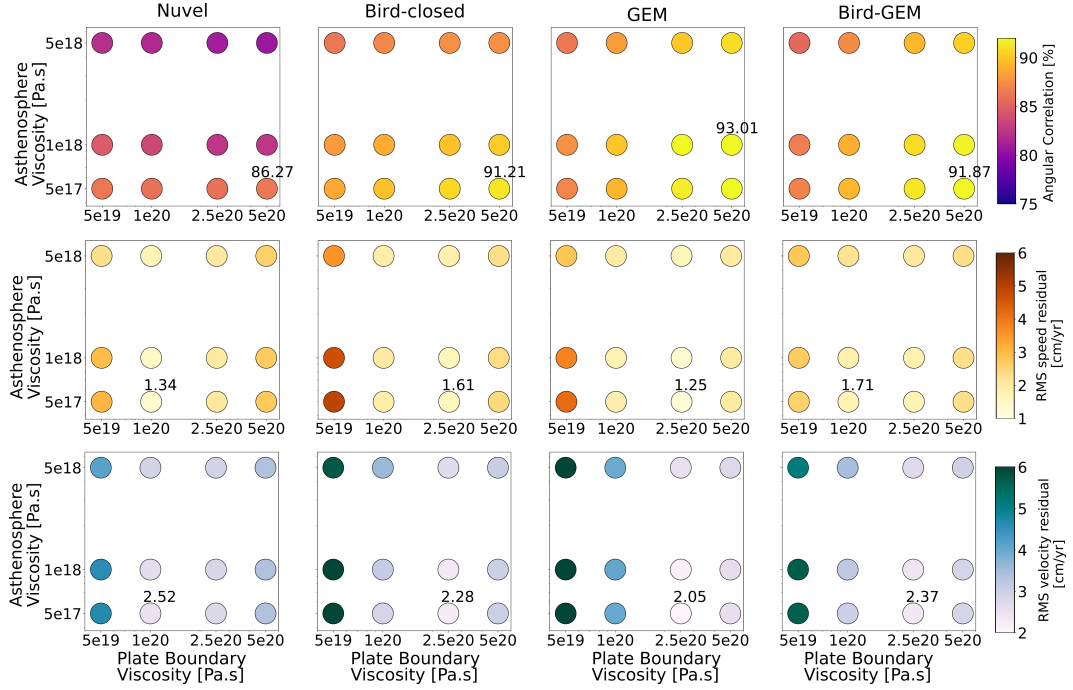


Figure 5. Angular correlation, mean speed residuals and velocity residuals between modeled and observed GPS velocities at the surface for different values of fault viscosities and asthenosphere viscosities for different plate boundary models (as in Figure 3). Maximum angular correlation, minimum speed residual, and minimum RMS velocity residual are annotated in each subplot. Note that in all plots light colors represent a good fit, and saturated colors represent significant misfits.

477

3.2 Influence of plate boundary geometry

478

479

480

481

482

483

484

485

486

487

488

489

490

491

492

493

494

495

In a second step, we picked a subset of parameter values close to the model that achieved the best fit to observed plate motions (Figure 4), specifically, plate boundary viscosities of 5×10^{19} to 5×10^{20} Pa s, and asthenosphere viscosities between 5×10^{17} and 5×10^{18} Pa s, and tested the influence of different plate boundary geometries (see Section 2.6.1). The resulting angular correlation, speed and RMS velocity residuals are shown in Figure 5. The choice of plate boundary model strongly influences the resulting plate motions (see also Figure 6) and therefore, the computed misfit (see Figures S2–S5 for maps of the velocity residuals). While the general trends we describe in Section 3.1 remain unchanged, we find an improved fit to the speed and a slightly better fit to the direction of plate motion. Specifically, the models based on the GEM database (GEM and Bird-GEM in Figure 3), which do not have closed plate boundaries, and which include information about the dip of plate boundaries, produce better weighted angular correlations for all models, reaching values around $\xi = 0.92$. The GEM plate boundaries also achieve the best overall fits indicated by the RMS velocity residual. Specifically, the best fitting model (with an RMS velocity residual of 2.05 cm/yr) has an asthenosphere viscosity of 5×10^{18} Pa s and a plate boundary viscosity of 2.5×10^{20} Pa s. However, all GEM models with plate boundary viscosities of 2.5×10^{20} Pa s reach good overall fits with RMS velocity residuals below 2.5 cm/yr.

496

497

498

499

500

501

502

503

504

505

506

507

508

509

510

511

512

513

514

515

516

517

518

519

520

521

522

523

524

525

526

527

528

529

These results show that the plate boundary geometry plays a crucial role for the direction of plate motions and that the presence of closed plate polygons in geodynamic models as implemented in previous mantle convection models (e.g., Stadler et al., 2010; Osei Tutu, Sobolev, et al., 2018; Liu & King, 2022) is not essential. It seems to be a better approximation of the plate boundary rheology to have clearly defined weak plate boundaries only in some regions (for example, at subduction zones and mid-ocean ridges), and more distributed deformation, where stress can be transferred between plates, in other places. Specifically, many regions where the plate boundaries are not closed in the Bird-GEM model and where the GEM model features regions with a diffuse fault network indicate what Bird (2003) labels as “orogens”, areas where deformation is complex and it is very difficult to define plates, because there is so much seismic, geologic, and geodetic evidence for distributed anelastic deformation. In the models based on the GEM database, weak zones in these complex regions only extend to crustal (seismogenic) depths, which achieves a better fit than the models with closed plate polygons. The Bird-closed and the Bird-GEM models do not perform as well as the GEM models, but better than Nuvel, and the residuals for their respective best-fit models are similar. This suggests that even without the diffuse fault network of the GEM database, discrete weak boundaries in the continental regions—as in the Bird-closed models—do not improve the modeled velocities considerably compared to a model that features strong continental regions with more distributed deformation, such as Bird-GEM. The Nuvel model, which is most commonly used for geodynamic models, performs substantially worse than the other plate boundary models, in particular in terms of angular fit. It can either fit the fast-moving oceanic plates, but then the slow motion of the South American and Antarctic plates is not reproduced well (see Figure S2, models with plate boundary viscosity of 10^{20} Pa s and asthenosphere viscosity of 10^{18} Pa s or below), or it fits the slower continental plates, but velocities are not high enough for the Pacific and Australian plates (models with plate boundary viscosity of 2.5×10^{20} Pa s or higher). The GEM, Bird-GEM, and Bird-closed models provide a reasonably good fit to all of these plates in the best-performing model (Figure 6), with in particular the Eurasian, North American and South American plate showing lower RMS residuals in the GEM model. On the other hand, many of the smaller plates in the Western Pacific that consistently show large RMS velocity errors in the Bird plate boundary models (Caroline, North Bismarck, South Bismarck) show an improved fit when using the Nuvel plate geometry, indicating that their rheology is better approximated by one large plate rather than several smaller ones.

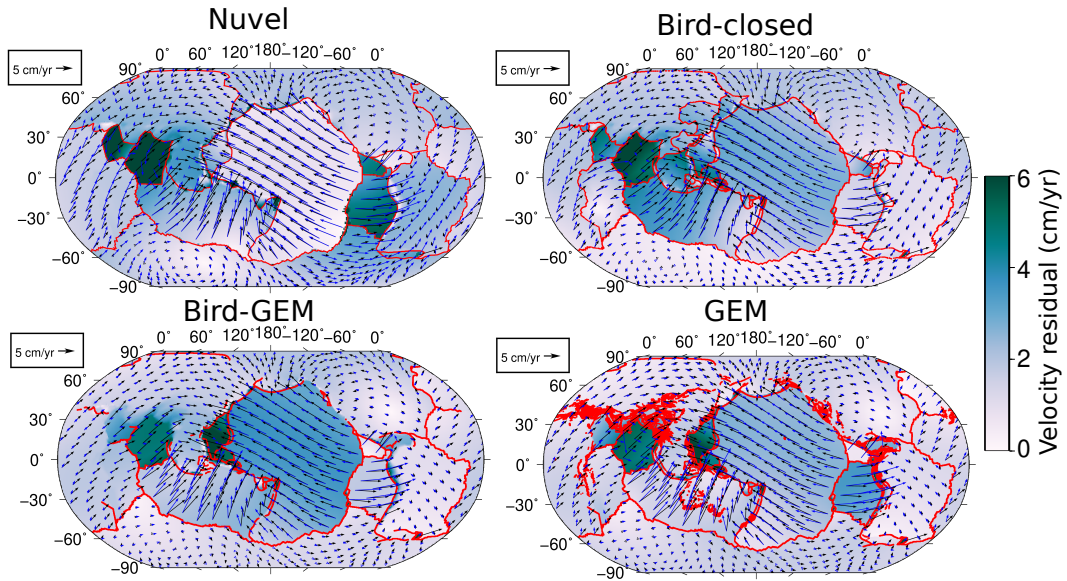


Figure 6. Velocity residual (background colors), together with the modeled velocity at the surface (blue arrows) and the observed GPS velocities (black arrows; Kreemer & Holt, 2001) for the different plate boundary models marked in red. For each plate boundary model, we show the model with the fault and asthenosphere viscosity values that achieve the lowest RMS velocity residual in our parameter study (Figure 5).

530 Our results indicate that different types of plate boundaries have different rheologies,
 531 and using a plate boundary model with closed polygons where all plate boundaries
 532 have the same strength is not a good approximation of plate tectonics on Earth. In par-
 533 ticular, assuming that subduction zones and mid-ocean ridges are substantially weaker
 534 than orogenic zones and continental rifts yields a better fit to global plate motions. This
 535 result is consistent with Osei Tutu, Sobolev, et al. (2018)’s analysis, who find an im-
 536 proved directional fit of most plates when using weaker subducting plate boundaries com-
 537 pared to the other plate boundaries.

538 3.3 Reference model

539 The model that fits the observed plate motions best uses the GEM plate geometry
 540 and has an asthenosphere viscosity of 5×10^{17} Pa s and a plate boundary viscos-
 541 ity of 2.5×10^{20} Pa s. This model features an RMS velocity residual of 2.05 cm/yr, an
 542 angular correlation of $\sim 91\%$ (94.5% in the measure of Becker, 2006; Liu & King, 2022)
 543 and a speed residual of 1.25 cm/yr. These values are comparable to previous studies (see
 544 below). The RMS velocity indicates that plates in our model are slightly slower than ob-
 545 served plate velocities, and the angular correlation shows a good fit to present-day plate
 546 directions. Comparing individual plates (Figure 6, bottom right) shows that the motion
 547 of the African, North American, South American and Eurasian plates are in good agree-
 548 ment with the observations, while most of the residual is concentrated in the smaller plates
 549 (Nazca, Indian, Philippines). The oceanic plates, and in particular the Pacific, Nazca
 550 and Cocos plate, have a very high correlation of the direction of plate motion (Figure 7,
 551 left). This is expected, since they are pulled in the direction of the slabs that are attached
 552 to them. On the other hand, they also have a low to moderate speed residual (Figure 7,
 553 right), with the Pacific plate moving slightly too slowly and the smaller Nazca plate mov-
 554 ing too fast. This could indicate that our chosen plate boundary viscosity is slightly too
 555 low compared to the asthenosphere viscosity, since smaller plates have a higher ratio of

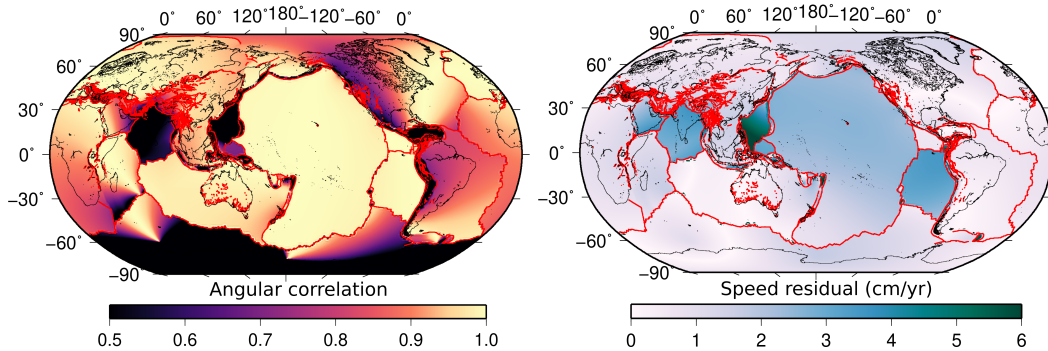


Figure 7. Map of angular correlation and speed residual for our reference model.

556 plate boundary length over area so that weak plate boundaries allow them to move quickly,
 557 especially if they are pulled by a slab (see Section 3.1). The Cocos plate is an exception,
 558 showing a good match with the observed GPS velocities both in direction and speeds.
 559 The Philippine plate does not fit this pattern either, having a poor fit both in terms of
 560 direction and speed of plate motion. This could be caused by a misalignment between
 561 the slab locations in our temperature model (which are vertically downward, based on
 562 the TM1 model) and the dipping weak zones in our plate model (which are dipping as
 563 recorded in the GEM database). Being attached to the Izu-Bonin/Mariana slab instead
 564 of or in addition to the Ryukyu and Manila slabs might cause the Philippine plate in our
 565 model to move much more slowly than observed.

566 In contrast to the oceanic plates, the continental plates exhibit a lower angular cor-
 567 relation, in particular the South American plate, the Indian plate, and the Antarctic plate.
 568 However, they have a small speed residual, in part also owing to their lower overall speed,
 569 causing them to contribute less to the global misfit of the plate motions.

570 Previous studies have achieved angular correlations in the range of 86–96%, sim-
 571 ilar to our value of $\sim 91.5\%$. Specifically, the angular correlation is between approximately
 572 86 and 88% in Conrad and Lithgow-Bertelloni (2002, Figure S1), $\xi = 0.95$ in the best-
 573 fit model of Becker (2006) that uses a laboratory-derived viscosity law, the angular mis-
 574 fit is around 10% and 8% in Alisic et al. (2012, Figure 4) and Osei Tutu, Sobolev, et al.
 575 (2018), respectively, and $\xi = 0.957$ in Liu and King (2022). We note that both Becker
 576 (2006) and Liu and King (2022) weigh their angular fits with the product of modeled
 577 and GPS velocities instead of using only the observed velocities as we do here. Using their
 578 measure of fit, our best-fit model has an angular fit of 94.5%. The speed of plate mo-
 579 tions is more difficult to compare, since different studies use different measures. In Conrad
 580 and Lithgow-Bertelloni (2002), the plate speed is a tuning parameter of the model, since
 581 it is normalized to the average plate speed by adapting the asthenosphere viscosity. Becker
 582 (2006) and Liu and King (2022) use the mean logarithmic amplitude ratio β to compare
 583 modeled and observed plate speed, and achieve $\beta \approx -0.22$ and $\beta = -0.047$, respec-
 584 tively. In this measure, $\beta = 0$ would indicate a perfect fit to the observed plate speed;
 585 and our best-fit model achieves a comparable fit of $\beta = -0.13$. We note that since β
 586 is calculated as $\sum_{i=1}^n \log_{10}(\mathbf{u}_i^{\text{model}}/\mathbf{u}_i^{\text{obs}})$, it is possible to have a small β value if some
 587 plates are faster and others slower than the observed speed, as long as they compensate
 588 each other in the mean, while our measure of the speed residual uses the absolute value
 589 of the difference between modeled and observed speeds before integrating over the sur-
 590 face (see Section 2.7). Osei Tutu, Sobolev, et al. (2018) report a root mean square ve-
 591 locity error of 38% (their fig 6, dark blue line), corresponding to a speed residual of 1.44
 592 cm/yr, slightly larger than our value of 1.25 cm/yr. Ghosh and Holt (2012) achieve an
 593 RMS misfit of ~ 1 cm/year, which is somewhat lower than our RMS residual of 2 cm/yr,

594 however, note that Ghosh and Holt (2012) assimilate observed deformation into their model
 595 setup by using a variable plate boundary viscosity proportional to the inverse of the ob-
 596 served strain rate. Both Stadler et al. (2010) and Alisic et al. (2012) use different mea-
 597 sures of evaluating their model fit, preventing us from performing a quantitative com-
 598 parison.

599 While the overall fit is similar to previous studies, one noteworthy point is that our
 600 models reproduce the motions of the North American plate well, something that has been
 601 difficult to achieve in previous modeling studies (Liu & King, 2022). Here, the key fea-
 602 ture that improves this fit is the use of the open (Bird-GEM or GEM) rather than closed
 603 plate boundaries along the western North American continent (Figure 6).

604 **3.3.1 Modeled strain rates**

605 To assess how well our best-fit model matches observed deformation rates, we com-
 606 pute the second invariant of the strain rate ($\dot{\epsilon}_{II}$) and compare it with the recent Global
 607 Strain Rate Model (GSRM; Kreemer et al., 2014) in Figure 8. Both modeled and ob-
 608 served $\dot{\epsilon}_{II}$ have characteristic types of deformation that can be classified into three dis-
 609 tinct categories: (1) slowly-deforming intraplate regions, (2) plate boundaries, and (3)
 610 regions of distributed deformation. The slowly-deforming intraplate regions feature low
 611 strain rates, in our model they are of the order $\sim 10^{-17} \text{ s}^{-1}$, in GSRM these are assumed
 612 to be rigid and not allowed to deform, i.e., the strain rate is not defined in these regions.
 613 Our modeled values are similar to the expected strain rates within a rigid lithosphere (Gordon,
 614 1998; Zoback et al., 2002), and are consistent with geodetic studies of stable intraplate
 615 regions (Calais & Stein, 2009; Braun et al., 2009) and previous global mantle convection
 616 models (Ghosh & Holt, 2012). The narrow zones of high deformation along the prescribed
 617 plate boundaries separating the rigid plates feature high strain rates, between 10^{-14} s^{-1}
 618 to 10^{-13} s^{-1} in our model and $\gtrsim 10^{-14} \text{ s}^{-1}$ in GSRM. Lithosphere with more distributed
 619 deformation has strain rates of the order of $\sim 10^{-16} \text{ s}^{-1}$. In our model, these zones are
 620 near the subducting plate boundaries between Nazca–South America, Pacific–Philippine,
 621 Cocos–North America, and Pacific–Australia, the continental–continental collision bound-
 622 ary between India–Eurasia, the transform boundaries between Pacific–North America,
 623 Scotia–South America, and the divergent boundaries between Somalia–Nubia, and Pacific–
 624 Antarctica. With the exception of Pacific–Antarctica, these zones were also defined as
 625 regions of broad deformation, which are not part of a rotating rigid plate, in GSRM (Figure
 626 1 in Kreemer et al., 2014). Several of these diffused deformation regions, i.e., along the
 627 Nazca–Pacific, India–Eurasia, Pacific–North America, and Pacific–Antarctica plates, are
 628 also labeled as “orogens” by Bird (2003). We do not attempt a more quantitative com-
 629 parison here since the width of our plate boundaries is limited by the achieved model
 630 resolution and does not necessarily correspond to the width of plate boundaries on Earth.
 631 But it is interesting to note that prescribing these diffuse weak zones only within the crust
 632 is enough to concentrate stresses from the lithosphere and deeper mantle at similar lo-
 633 cations as observed on Earth (Figure 8)—a result of the heterogeneous viscosity distri-
 634 bution including lateral variations in temperature and lithospheric thickness.

635 **3.3.2 Model resolution**

636 To test how our numerical resolution impacts the results, we rerun our reference
 637 model with 4 global and 4 adaptive refinement levels instead of 5 + 2 refinements as used
 638 for all other models in this study. This increases the resolution in the uppermost man-
 639 tle and at the plate boundaries to 8.5 km, while maintaining a lower mantle resolution
 640 comparable with the input tomography model. Overall, the results of the higher-resolution
 641 model are very similar to our reference model: an angular correlation of 90.5% (refer-
 642 ence model: 91%), a mean speed residual of 1.38 cm/yr (reference: 1.25 cm/yr), and a
 643 RMS velocity residual of 2.15 cm/yr (reference: 2.05 cm/yr). While we do not observe
 644 significant differences in the computed misfits between our standard and the high-resolution

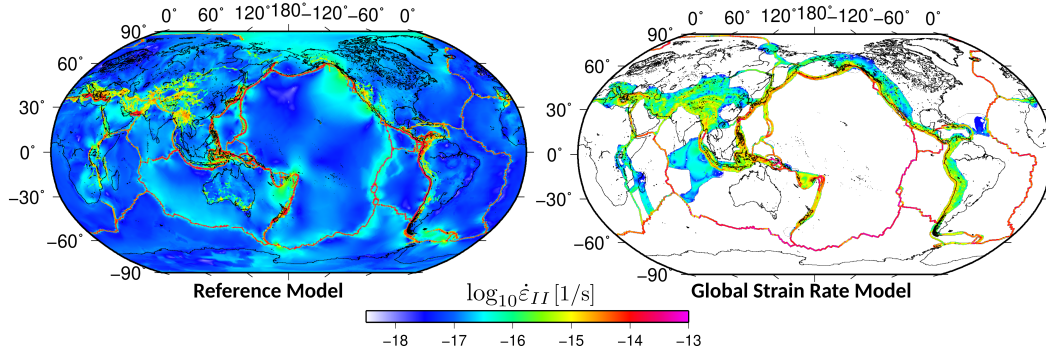


Figure 8. Modeled second invariant of strain rate at the surface for our reference model (left) and from the GSRMv2.1 model (Kreemer et al., 2014).

645 model, the plates tend to move slightly slower in the high-resolution model. The fact that
 646 differences between model resolutions are very small shows that our results are robust
 647 with respect to the numerical resolution of the models. We note that in order to keep
 648 the results comparable, the width of plate boundaries in the high-resolution model is still
 649 the same as in our base model, and larger than the width of lithospheric shear zones on
 650 Earth. Reducing this width may affect the model results, and could provide additional
 651 insights into plate boundary stresses and rheology in future studies.

652 3.4 Varying slab and craton strength

653 As outlined in the previous section, the model configuration with the GEM plate
 654 boundaries, an asthenosphere viscosity of 5×10^{17} Pa s, and a plate boundary viscosi-
 655 ty of 2.5×10^{20} Pa s achieves the lowest RMS velocity misfit. We therefore use this model
 656 as a reference case to test the influence of additional parameters.

657 For this purpose, we include neutrally buoyant and stiff cratons as described in Sec-
 658 tion 2.6.3 in our reference model. We then compare the resulting plate motion fit with
 659 the original (reference) model (Figure S7). Our results show that the modeled plate ve-
 660 locities in the presence of cratons are only marginally slower than the reference model.
 661 Slow-down occurs in particular for the plates that contain cratons. On the other hand,
 662 the direction of plate motion is similar to our reference model (see also Table 3). These
 663 results suggest that the lithospheric viscosity derived from the colder regions of cratons
 664 in our reference model is already strong enough to resist almost all deformation within
 665 the continental lithosphere and further increasing the viscosity in the cratonic lithosphere
 666 does not affect the plate-mantle coupling. Since lithospheric thickness is the same in the
 667 models with and without cratons, this also indicates that the observed anti-correlation
 668 between plate speed and continental area (Forsyth & Uyeda, 1975) is predominantly re-
 669 lated to the thinner asthenosphere associated with thick cratonic roots rather than in-
 670 creased friction between the asthenosphere and the base of the plate. Our results are con-
 671 sistent with Ghosh et al. (2013), who find a similar global fit to the observed plate mo-
 672 tions for models with strong cratons and models with temperature-dependent viscosity,
 673 and with the study of Conrad and Lithgow-Bertelloni (2006), who find that the basal
 674 tractions on a lithosphere with lateral viscosity variations are similar to those of a litho-
 675 sphere with only a layered viscosity structure. We do not investigate the effects of vary-
 676 ing craton thickness on the plate motions, which will likely change the plate-mantle cou-
 677 pling as observed in previous studies (Zhong, 2001; Conrad & Lithgow-Bertelloni, 2006;
 678 Rolf & Tackley, 2011). However, we study the influence of the overall lithospheric thick-
 679 ness (see Supporting Information).

680 In a separate test, we investigate the influence of stress transfer within slabs in the
 681 asthenosphere (see Section 2.6.3). In contrast to the reference model, this configuration
 682 does not include the cold regions of the asthenosphere (more than 100 K below the adi-
 683 abat) when scaling viscosities to adhere to the radial viscosity profile on average. Con-
 684 sequently, subducted slabs, but also cold cratonic roots, have a higher viscosity compared
 685 to the reference case, potentially allowing for better transmission of stresses within sub-
 686 ducted slabs.

687 The presence of stiffer cratons and well-connected slabs increases the overall speed
 688 of the plates and leads to an improved angular correlation and RMS velocity residual
 689 compared to the reference model (see Table 3). This suggests that the effect of improved
 690 stress transmission in the stronger slabs slightly surpasses the increased viscous drag around
 691 the cold regions, and consequently leads to faster motion of plates and better directional
 692 fit to the observations. This is illustrated by the modeled velocities at the surface and
 693 along a cross-section cutting through the subducted Nazca slab (Figure 9): The higher
 694 viscosity in cold asthenospheric regions in this model (compared to the reference model)
 695 improves the connectivity of slabs throughout the asthenosphere, leading to higher slab
 696 sinking velocities below the asthenosphere and slightly higher plate velocities. The most
 697 substantial velocity increase occurs in the Pacific and Cocos plate, whereas other oceanic
 698 plates (Australia and Nazca) do not show higher velocities. The directional change is most
 699 significant for the South American and Nazca plates, both aligning better with the ob-
 700 served GPS velocities in the presence of stronger slabs.

701 Previous studies (Billen & Hirth, 2007; Capitanio et al., 2009) have suggested that
 702 stiff slabs, or a stiff slab core, with a viscosity of $10^{24} - 10^{25}$ Pa s, are essential to ac-
 703 curately model plate motions. This strong stress guide is required for transmitting slab
 704 pull forces effectively (>70%) through the slab to the subducting plate (Capitanio et al.,
 705 2009), and for achieving a high “plateness” of surface velocities (Zhong et al., 1998). The
 706 high subducting to nonsubducting plate speed ratio observed on Earth can only be re-
 707 covered if the buoyancy of upper-mantle slabs is transferred to the plates by slab pull
 708 forces rather than slab suction (Conrad & Lithgow-Bertelloni, 2004). However, the in-
 709 crease in oceanic plate speed due to stronger slabs in our models is much smaller than
 710 the about two-fold increase in slab pull in presence of a stiffer slab core predicted by Capitanio
 711 et al. (2009). In our models, slabs are not as well-defined as in time-dependent geody-
 712 namic models of subduction evolution, (1) because we use a tomographic model that to
 713 some degree diffuses the temperature anomaly of slabs so that they are too wide and not
 714 cold enough, and (2) because our model includes a boundary between two different tem-
 715 perature models at 200 km depth, where slabs are not always well-connected. This re-
 716 duces the potential for stress transfer along the slab, even if colder regions are more vis-
 717 cous. In addition, the more diffused temperature anomalies counteract one of the key
 718 mechanisms that Billen and Hirth (2007) identified for keeping the subducting plate and
 719 overriding plate decoupled and allowing slabs to easily subduct through the upper man-
 720 tle: A reduced viscosity around the slab due to the strain-rate dependence of viscosity.
 721 In tomography-based models, temperatures are reduced in a broader region around slabs,
 722 leading to wider zones of increased viscosity and suppressing strain localization around
 723 the slab. This is one of the main weaknesses of tomography-based instantaneous mod-
 724 els and highlights the need for incorporating better slab models into this type of sim-
 725 ulation.

726 To better understand this effect of slab connectivity, we vary the transition depth
 727 between the TM1 model and the tomography model in the reference model setup (from
 728 200 km to values between 100 and 300 km, see Table 3). Shallower transition depths im-
 729 ply more connected but diffused slabs (see Section 2.3), whereas deeper transitions im-
 730 ply more defined, but vertical slabs in the uppermost mantle that might be disconnected
 731 at the boundary between the two temperature models. We find that the model with a
 732 transition depth of 150 km achieves a better fit to the observed plate motions than the

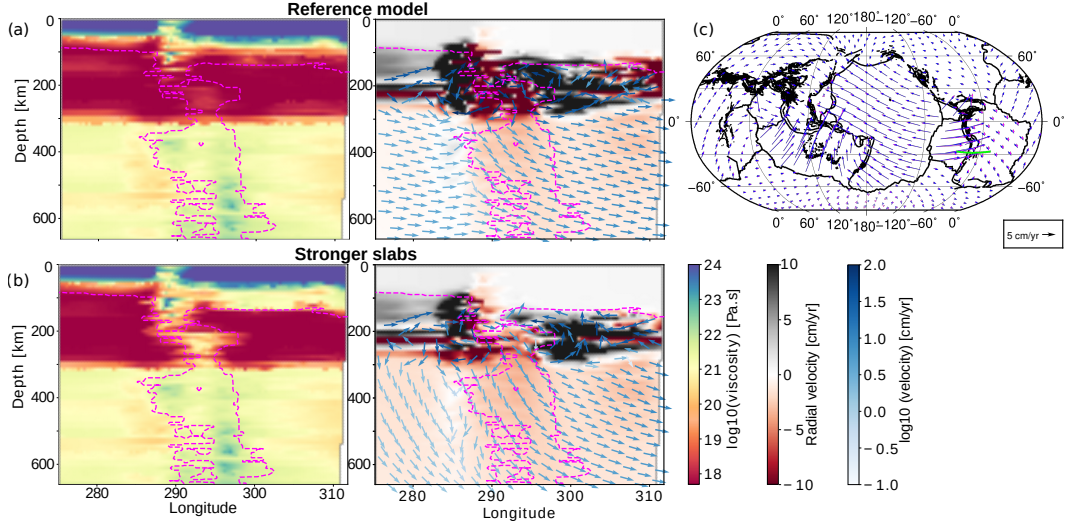


Figure 9. Viscosity distribution and flow field in the upper mantle and transition zone through the Andes subduction zone for the reference model (a) and the model with strong slabs and cratons in the asthenosphere (b). Magenta contours represent the approximate slab and plate location as regions where the non-adiabatic temperature is < -100 K. For clarity, velocity vectors are only plotted below 150 km depth. (c) Modeled velocity at the surface for our reference model (blue) and the model with stiffer slabs and cratons (magenta). The green line marks the location of the cross-section plotted in (a) and (b).

733 reference model, with a velocity residual of 1.87 cm/yr (compared to 2.05 cm/yr). The
 734 main improvement in this model compared to the reference model is the increased speed
 735 of the Pacific plate, which is now comparable to the observations. In addition, the Philip-
 736 pine plate now moves in the correct direction, and the angular correlation for South Amer-
 737 ica is improved as well. On the other hand, the speed residuals increase for the Nazca
 738 and Cocos plate because they are now moving faster than observed (Figure 10), and the
 739 angular correlation of the North American Plate is lower. The higher speed of the oceanic
 740 plates is likely due to the better slab connectivity when using a transition depth of 150
 741 km instead of 200 km, as in our reference model. Accordingly, this model is the best-
 742 fitting model amongst all the model configurations we tested in this study (see Tables
 743 3 and S2). We note that other plate boundary configurations such as Bird and Bird-GEM
 744 achieve the best fit for a transition depth of 200 km instead of 150 km (see Table S1),
 745 which is what motivated us to use the value of 200 km for our parameter study presented
 746 in Section 3.1.

747 3.5 Quantifying plate driving forces

748 In addition, we use our reference model to study how much each of the different
 749 components of the model contributes to the observed plate motion. For this purpose, we
 750 separately remove buoyancy and viscosity variations from the tomography model (be-
 751 low 200 km depth, TM1_only model), and from the sublithospheric upper mantle above
 752 300 km depth (LLNL_only model).

753 3.5.1 Influence of upper mantle heterogeneities

754 Without the driving forces in the transition zone and lower mantle introduced by
 755 the tomography model, the plate speed is reduced to about 73% of the reference model,

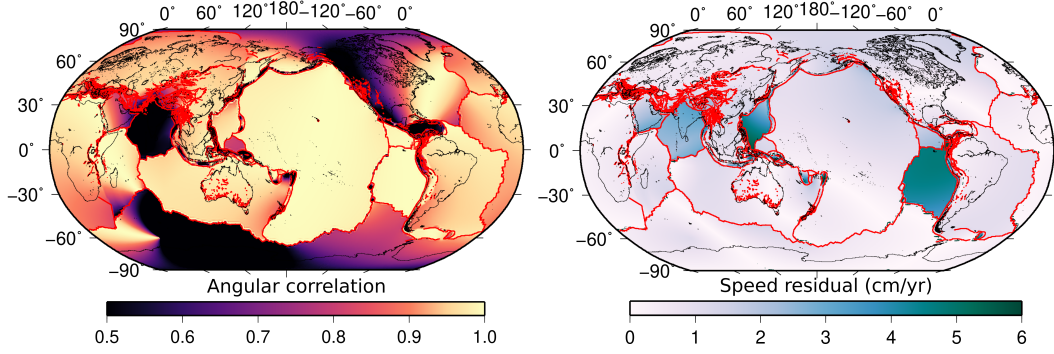


Figure 10. Map of angular correlation and speed residual for our best-fit model.

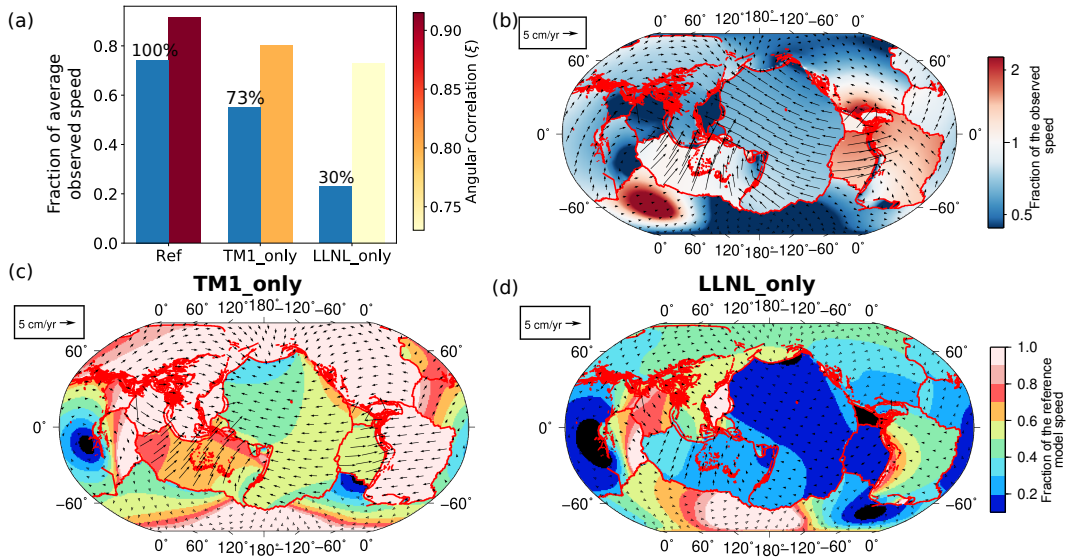


Figure 11. (a) The ratio of averaged modeled speed to averaged observed GPS speed (blue bars) for different models and their respective angular correlation-like measure, ξ . The text on the bars denotes the fraction of average modeled speed relative to average reference model speed. (b) Point-wise fraction of modeled speed in the reference model with respect to the observed GPS speed. (c, d) Point-wise fraction of the modeled speed with respect to our reference model for two models: (c) Model with temperatures based on only the TM1 model above 200 km depth and with a homogeneous mantle below (TM1_only). (d) Model with temperatures based on only the LLNL-G3D-JPS model below 300 km depth and a homogeneous sublithospheric mantle above (LLNL_only).

756 on average. This means that about three quarters of the observed plate speed can be ex-
 757 plained by the forces resulting from heterogeneous mantle structure in the uppermost
 758 200 km of the Earth alone. The velocity reduction associated with removing the man-
 759 tle structure below 200 km is much stronger in the oceanic plates compared to the con-
 760 tinental plates (Figure 11c), indicating that the lower plate speed is caused by a reduc-
 761 tion mostly in slab pull forces. While slab pull only acts on subducting plates, slab suc-
 762 tion acts equally on all plates (or might have a slightly bigger influence on continental
 763 plates due to the higher traction at the plate base). Consequently, a change in slab pull
 764 should primarily affect subducting plates, whereas a change in slab suction would affect
 765 all plates similarly. But with the exception of the African plate, which is slowed down
 766 substantially ($\sim 40\%$ to 50% of the reference model), continental plates speed up or re-
 767 tain most of their speed (Figure 11c). We also attribute this to the low-temperature re-
 768 gions below continental plates generated by cold subducting slabs. These low-temperature
 769 regions lead to strong viscous drag at the base of the plate if the heterogeneous man-
 770 tle structure below 200 km depth is included. If these drag forces are reduced by using
 771 a homogeneous mantle below 200 km depth, the plates can move more easily. On the
 772 other hand, the African plate, which has no plate subducting beneath it, does slow down.
 773 Oceanic plates that have a slab attached to them, except Australia, move only about half
 774 as fast in the model with the homogeneous lower mantle, despite still being connected
 775 to the slabs prescribed in the TM1 model up until a depth of 200 km. The angular cor-
 776 relation of the predicted plate motions decreases as well from 91.5% to about 80% .

777 *3.5.2 Influence of lower mantle heterogeneities*

778 Without the driving forces from slabs in the asthenosphere, our models retain about
 779 30% of their plate speed. Again, this velocity reduction is stronger in the oceanic plates
 780 (which retain $10\text{--}30\%$ of their speed) compared to the continental plates (which retain
 781 $40\text{--}50\%$ of their speed). The angular correlation decreases considerably from 91.5% to
 782 73.6%). Note that the removal of asthenospheric temperature anomalies has a two-fold
 783 effect on plate velocities. First, it removes the driving forces from slab buoyancy; sec-
 784 ond, it removes the higher viscosities that help transfer deeper buoyancy forces to the
 785 surface and influence plate motions. Since the density anomalies below 300 km are no
 786 longer connected to the plates at the surface, all driving forces in this model result from
 787 slab suction/viscous drag and lithospheric structure. Consequently, these forces together
 788 explain at least 30% of the speed of plates, with the remaining $\leq 70\%$ being associated
 789 with slab pull and the associated stress transfer within slabs.

790 *3.5.3 Comparison to previous studies*

791 The importance of lower mantle versus upper mantle driving forces has been de-
 792 bated in previous studies.

793 In the study of Osei Tutu, Sobolev, et al. (2018), lower mantle heterogeneities are
 794 critical to reproducing plate motions. The angular misfit in their models increases from
 795 less than 10% to up to 50% without the density anomalies in the lower mantle, with the
 796 largest misfit occurring for the highest friction at plate boundaries. They also estimate
 797 that the tractions resulting from buoyancy below 300 km depth provide about 70% of
 798 the plate driving force. Conversely, when upper mantle heterogeneities are removed, their
 799 models only show a decrease in the root mean square velocity of approximately 20% , re-
 800 taining about 80% of the plate speed and featuring only a small reduction in the direc-
 801 tional fit.

802 On the other hand, the models of Stadler et al. (2010) fit observed plate motions
 803 best without including lower mantle heterogeneities at all. They prescribe subducted slabs
 804 as high-viscosity stress guides based on seismicity, and find that extending them into the
 805 lower mantle causes overall mantle flow velocities and most oceanic plate velocities to

806 decrease, making convergent velocities at trenches more symmetric. Similarly, the mod-
 807 els of Alisic et al. (2012) show that increasing lower mantle temperature variations speeds
 808 up overriding plates that are not attached to subducting slabs and slows down subduct-
 809 ing plates with slabs that connect to large-wavelength cold anomalies of high viscosity
 810 in the lower mantle, such as the Pacific and Australian Plate. However, Alisic et al. (2012)
 811 conclude that lower mantle heterogeneities promote an overall increase in plate speeds,
 812 in contrast to Stadler et al. (2010).

813 Conrad and Lithgow-Bertelloni (2002) find that observed plate motions are best
 814 predicted if slabs in the upper mantle generate slab pull forces that account for about
 815 half of the total driving force on plates. Their models best reproduce present-day plate
 816 motions if nearly the entire weight of upper mantle slabs contributes to the slab pull force,
 817 but lower mantle slabs contribute to slab suction, being supported by viscous mantle forces.
 818 If lower mantle slabs contribute to slab pull as well, the directions and relative speeds
 819 of individual plates are poorly reproduced. Similarly, Becker and O’Connell (2001) con-
 820 clude that both upper and lower mantle driving forces are important, but find a slightly
 821 lower contribution of the lower mantle: Out of the total driving forces, they attribute
 822 20–35% to lower mantle buoyancy, 40–60% to upper mantle buoyancy, and 10–30% to
 823 lithospheric structure/ridge push (Figure 19 in their study). This means that out of the
 824 total mantle contribution of 70–90%, roughly 40% comes from lower mantle heterogeneities.
 825 However, in contrast to Conrad and Lithgow-Bertelloni (2002), Becker and O’Connell
 826 (2001) find that the angular fit to the observations improves if the viscous drag from upper-
 827 mantle slabs acts on both overriding and subducting plates rather than one-sided pull
 828 on the subducting plate (their Figure 20).

829 The differences between studies can be explained by the different rheological prop-
 830 erties employed and the associated balance between plate driving forces. The narrow,
 831 high-viscosity slabs in Stadler et al. (2010) are prescribed based on seismicity rather than
 832 a seismic tomography model, allowing an effective transmission of stresses between the
 833 slab tip and the subducting plate. Since we know that the lower mantle is heterogeneous,
 834 the deteriorating fit in the models where slabs extend to the lower mantle could indicate
 835 that these modeled slabs transmit stresses to a higher degree than the slabs in the Earth’s
 836 mantle. This reasoning is also consistent with the conclusion of Conrad and Lithgow-
 837 Bertelloni (2002) that plate motions are fit best if lower mantle slabs contribute to slab
 838 suction but not slab pull. The models of Osei Tutu, Sobolev, et al. (2018) use a Drucker-
 839 Prager rheology, which is strongly nonlinear. Consequently, a slight reduction in driv-
 840 ing forces can cause a large change in viscosity if it causes stresses to fall below the yield
 841 strength of the material. Because of this nonlinear feedback, mantle tractions can influ-
 842 ence the strength of plate boundaries: Only when the stresses excited by the driving forces
 843 exceed the yield strength of the material, plate boundaries are weak and allow for plate-
 844 like motion. This explains why the reduction in driving forces causes a strong increase
 845 in angular misfit, which is not the case in more linear models. In addition, the strong
 846 impact of lower mantle heterogeneities compared to upper mantle slabs is likely related
 847 to a different balance between suction and slab pull force in their models. Apart from
 848 the use of a visco-elastic-plastic rheology, Osei Tutu, Sobolev, et al. (2018) also use a slightly
 849 higher asthenospheric viscosity than in our best-fit model, which allows tractions caused
 850 by slab suction to transmit higher stresses to the plates. More importantly, Osei Tutu,
 851 Sobolev, et al. (2018) do not include lateral viscosity variations below 300 km depth, and
 852 they employ an averaged tomography model (SMEAN, Becker & Boschi, 2002), which
 853 by nature features subducted slabs as broad structures. Consequently, slabs in their mod-
 854 els cause a strong buoyancy force, but do not increase mantle viscosity, allowing them
 855 to sink faster and incite more mantle flow than in a model with temperature-dependent
 856 viscosity.

857 This phenomenon was already noted in Stadler et al. (2010), who found that plate
 858 velocities approximately double (their table S4, Figure S5) when temperature-dependence
 859 of viscosity in the lower mantle is neglected.

860 Our models improve on existing studies by including lateral viscosity variations in
 861 the lower mantle, and at the same time using the LLNL-G3D-JPS tomography model
 862 that features more clearly defined slab structures in the lower mantle compared to pre-
 863 vious studies.

864 Our estimate on the amount of the slab pull force of $\leq 70\%$ is consistent with Conrad
 865 and Lithgow-Bertelloni (2004), who find that slab pull provides 60-80% of the plate driv-
 866 ing force, depending on the asthenosphere viscosity.

867 Our results also agree with the study of Conrad and Lithgow-Bertelloni (2002), who
 868 find that models with only slab suction still achieve a reasonable ($\sim 80\%$) angular cor-
 869 relation, but do not reproduce the observed relative speed between the different plates.

870 To estimate the balance of forces acting on the North American plate in particu-
 871 lar, Liu and King (2022) test scenarios that either only include buoyancy from seismic
 872 tomography (in this case the S40RTS model) throughout the whole mantle, or, alterna-
 873 tively, replace fast seismic anomalies from 100 to 660 km depth by a global model of re-
 874 gionalized upper mantle slabs inferred from seismicity. They find that plate motions pre-
 875 dicted from S40RTS alone are somewhat slower than in models that include slabs based
 876 on seismicity, but the directions generally fit observed plate motions well ($\xi = 0.858$).
 877 However, the direction of oceanic plates is predicted substantially better than that of the
 878 continental plates, with in particular the North American Plate moving in the opposite
 879 direction as observed. Based on these results, Liu and King (2022) argue that buoyancy
 880 derived from seismic tomography alone is not sufficient to predict the motion of conti-
 881 nental plates in general and the North American plate in particular. Instead, they find
 882 the best fit to the North American plate motion when they remove the buoyancy below
 883 660 km depth and additionally reduce the seismic-velocity-to-density scaling in seismi-
 884 cally slow regions to account for the presence of partial melt.

885 This result is consistent with our model with laterally homogeneous buoyancy be-
 886 low 200 km (TM1_only), where the North American plate fits the observed velocity bet-
 887 ter than in our best-fit model both in direction and magnitude (Figure 11c). As in Liu
 888 and King (2022), our models also show a decrease in the general directional fit (from 91.5%
 889 to 74%) when only tomography-derived density anomalies are included, and only below
 890 200 km depth (Figure 11a and d). However, a model setup closer to that of Liu and King
 891 (2022), where the transition from the TM1 model to tomography occurs at 100 km depth,
 892 features a similar angular fit as our reference model (91.6%; see Table 3). We attribute
 893 this good fit in our model even with seismic tomography alone to the better resolution
 894 of the LLNL-G3D-JPS compared to S40RTS used by Liu and King (2022), leading to
 895 coherent slabs in our models.

896 We note that all estimates for the relative percentage of forces have large uncer-
 897 tainties, because they depend on the asthenosphere and plate viscosities. The lower the
 898 asthenosphere viscosity, the bigger the effect of slab pull compared to suction (Conrad
 899 & Lithgow-Bertelloni, 2004). Our models show trade-offs between the two parameters,
 900 and they achieve a similar velocity residual for a range of parameter values. In addition,
 901 the force balance also depends on the scaling of seismic velocity to density, and on the
 902 lower mantle viscosity, since increased lower mantle viscosity increases the importance
 903 of slab pull over slab suction. However, our results in comparison to previous studies il-
 904 lustrate the importance of the coupling between upper-mantle and lower-mantle driv-
 905 ing forces of plate tectonics. Particularly relevant seems to be the continuity of subducted
 906 slabs and their potential to act as stress guides, and the presence of lateral viscosity vari-
 907 ations throughout the whole mantle.

Table 3. Misfit of various model configurations based on our reference case

| Model name | Angular correlation (%) | Mean speed residual (cm/yr) | RMS velocity residual (cm/yr) |
|--|-------------------------|-----------------------------|-------------------------------|
| Reference model* | 91.5 | 1.25 | 2.05 |
| TM1 to LLNL-G3D-JPS transition at 300 km | 87.27 | 1.50 | 2.65 |
| TM1 to LLNL-G3D-JPS transition at 150 km | 93.18 | 0.90 | 1.87 |
| TM1 to LLNL-G3D-JPS transition at 100 km | 91.6 | 1.39 | 2.67 |
| TM1 model depths +30 km (see SI) | 90.33 | 2.02 | 2.71 |
| TM1 model depths -30 km (see SI) | 51.27 | 13.9 | 29.04 |
| Homogeneous tomography | 79.8 | 2.05 | 3.18 |
| Homogeneous sub-lithospheric mantle until 300 km | 73.63 | 2.97 | 3.87 |
| Increased craton strength | 91.68 | 1.3 | 2.09 |
| Increased slab strength | 93.33 | 1.19 | 1.92 |
| Grain size = 1.4 mm (see SI) | 93.28 | 1.38 | 2.15 |
| Constant Vs-to-T scaling (see SI) | 91.5 | 1.17 | 2 |
| Reference model (higher resolution) | 90.6 | 1.38 | 2.16 |

*Reference model uses GEM plate boundaries, a plate boundary viscosity of 2.5×10^{20} Pa s and an asthenosphere viscosity of 5×10^{17} Pa s.

4 Conclusions

We have used instantaneous 3-D mantle convection simulations with a heterogeneous density and viscosity structure inferred from the LLNL-G3D-JPS tomography model to study the effects of plate driving and resisting forces on the observed surface deformation. In particular, we investigated the influence of varying friction at the plate boundaries and the base of the plates, different plate boundary geometries, and different upper-mantle viscosity structure defining slabs, cratons and the lithosphere. We find that both the frictional forces at plate boundaries and the base of plates and slab pull have a strong influence on the plate motions. In particular, plate boundaries that are 3 to 4 order of magnitude weaker than the surrounding lithosphere, and an intermediate to low asthenosphere viscosity of 5×10^{17} to 5×10^{18} Pa s lead to a reasonable fit to the observed GPS data both in terms of direction and speed of plate motion (Figure 5). Additionally, our models demonstrate that the choice of plate boundary geometry is critical for the direction of plate motions and affects which plates fit the observations well. Specifically, models based on the GEM database with open plate boundaries, dipping discrete (lithospheric depth) weak zones in the oceans and more diffused (crustal depth) weak zones within the continents achieve the lowest overall RMS velocity residuals relative to the observations (Figure 6). Our models also reaffirm the importance of slab pull for plate tectonics, showing that slab pull in the uppermost mantle (at depths <300 km) contributes more than half of the observed speed of plate motions (Figure 11), and that it is crucial for slabs to be connected to be able to transfer forces to the plate. Models without slab pull can only explain about 30% of the average plate speed. Using different temperature models for the lithosphere/upper mantle and the lower mantle (e.g. based on tomography) can easily lead to gaps in the slab structure, reducing the amount of slab pull being transferred to the plate.

The improved fit of the GEM models compared to models with closed plate boundaries (Figure 6) suggests two important physical properties of the plate boundaries on

935 Earth that should be considered in global mantle convection models: First, plate bound-
936 aries are not uniformly weak everywhere, and they do not have to be closed polygons.
937 They are better described by using discrete, weak zones cutting through the whole litho-
938 sphere only in the oceanic regions, and instead a network of intra-plate faults down to
939 the depth defined by seismicity in the continents, leading to plate boundaries that are
940 not as weak as in the oceans and consequently more distributed deformation. Variable
941 plate boundary viscosities have also been included in previous modeling studies to im-
942 prove the plate motion fits regionally (Stadler et al., 2010; Alisic et al., 2012) or glob-
943 ally (Ghosh & Holt, 2012). However, the variability in the strength of plate boundaries
944 is either based on observed strain rates (Ghosh & Holt, 2012), which is already a result
945 of the deformation produced due to plate-driving forces and does not provide a phys-
946 ical explanation for why the strength varies, or is only included at one plate boundary
947 (between the Nazca and South America in Stadler et al. (2010); Alisic et al. (2012)’s mod-
948 els). Second, it is important to include the dip angle of plate boundaries—as in the GEM-
949 based models—rather than using vertical shear zones. This allows the slab pull forces
950 to be transferred more efficiently to the subducting plate at the surface because the shear
951 zones follow along the upper boundary of the subducting plate rather than cutting through
952 it, and the deformation between the plates occurs at an angle that allows horizontal stresses
953 to be transferred more easily.

954 Acknowledgements

955 We thank Anthony Osei Tutu for providing the TM1 temperature model used in
956 this study, and the authors of LLNL-G3D-JPS tomography model for making their model
957 publicly available. We would also like to thank Wolfgang Bangerth, John Naliboff, Shangxin
958 Liu and Anthony Osei Tutu for insightful discussions and feedback on this study.

959 We thank the Computational Infrastructure for Geodynamics (geodynamics.org)
960 which is funded by the National Science Foundation under award EAR-0949446 and EAR-
961 1550901 for supporting the development of ASPECT. AS, RG and JD were supported
962 by the NSF grant EAR-1925677.

963 This work used the Extreme Science and Engineering Discovery Environment (XSEDE),
964 which is supported by National Science Foundation grant number ACI-1548562. Com-
965 pute time was provided by CIG on the NSF-funded cluster EXPANSE, operated by the
966 San Diego Supercomputer Center at UC San Diego. The authors acknowledge the Texas
967 Advanced Computing Center (TACC, <http://www.tacc.utexas.edu>) at The University
968 of Texas at Austin for providing high-performance computing resources on Frontera (Stanzione
969 et al., 2020) that have contributed to the research results reported within this paper. The
970 authors also acknowledge University of Florida Research Computing (<https://www.rc.ufl.edu/>)
971 for providing additional computational resources and support that have contributed to
972 the research results reported in this publication.

973 5 Data Availability

974 All models presented in the study are run using ASPECT version 2.4.0-pre (com-
975 mit 7ee6c0ec6), which is freely available on Github (Kronbichler et al., 2012; Heister et
976 al., 2017; Bangerth et al., 2022b, 2022a), compiled with the deal.II version 9.4.0. We use
977 the branch https://github.com/alarshi/WorldBuilder/tree/rounded_fault in World
978 builder to incorporate smooth viscosity transition from fault viscosity to lithospheric vis-
979 cosity. We provide our material model plugin and all data necessary to reproduce our
980 results as a data publication on Zenodo (Saxena et al., 2022).

981 **References**

- 982 Alisic, L., Gurnis, M., Stadler, G., Burstedde, C., & Ghattas, O. (2012). Multi-scale
 983 dynamics and rheology of mantle flow with plates. *Journal of Geophysical Re-*
 984 *search: Solid Earth*, *117*(B10).
- 985 Alisic, L., Gurnis, M., Stadler, G., Burstedde, C., Wilcox, L. C., & Ghattas, O.
 986 (2010). Slab stress and strain rate as constraints on global mantle flow. *Geo-*
 987 *physical Research Letters*, *37*(22).
- 988 Arndt, D., Bangerth, W., Blais, B., Fehling, M., Gassmüller, R., Heister, T., ... oth-
 989 ers (2021). The deal. ii library, version 9.3. *Journal of Numerical Mathematics*,
 990 *29*(3), 171–186.
- 991 Artemieva, I. M. (2006). Global 1×1 thermal model tc1 for the continental litho-
 992 sphere: implications for lithosphere secular evolution. *Tectonophysics*, *416*(1-
 993 4), 245–277.
- 994 Balázs, A., Matenco, L., Vogt, K., Cloetingh, S., & Gerya, T. (2018). Extensional
 995 polarity change in continental rifts: Inferences from 3-d numerical modeling
 996 and observations. *Journal of Geophysical Research: Solid Earth*, *123*(9),
 997 8073–8094.
- 998 Bangerth, W., Dannberg, J., Fraters, M., Gassmoeller, R., Glerum, A., Heister, T.,
 999 ... Naliboff, J. (2022a, July). ASPECT: *Advanced Solver for Problems in*
 1000 *Earth’s ConvecTion, User Manual*. (doi:10.6084/m9.figshare.4865333) doi:
 1001 10.6084/m9.figshare.4865333
- 1002 Bangerth, W., Dannberg, J., Fraters, M., Gassmoeller, R., Glerum, A., Heis-
 1003 ter, T., ... Naliboff, J. (2022b, July). *Aspect v2.4.0*. Zenodo. doi:
 1004 10.5281/zenodo.6903424
- 1005 Becker, T. W. (2006). On the effect of temperature and strain-rate dependent vis-
 1006 cosity on global mantle flow, net rotation, and plate-driving forces. *Geophysical*
 1007 *Journal International*, *167*(2), 943–957.
- 1008 Becker, T. W., & Boschi, L. (2002). A comparison of tomographic and geodynamic
 1009 mantle models. *Geochemistry, Geophysics, Geosystems*, *3*(1).
- 1010 Becker, T. W., & O’Connell, R. J. (2001). Predicting plate velocities with mantle
 1011 circulation models. *Geochemistry, Geophysics, Geosystems*, *2*(12).
- 1012 Billen, M. I., & Hirth, G. (2007). Rheologic controls on slab dynamics. *Geochem-*
 1013 *istry, Geophysics, Geosystems*, *8*(8).
- 1014 Bird, P. (2003). An updated digital model of plate boundaries. *Geochemistry, Geo-*
 1015 *physics, Geosystems*, *4*(3).
- 1016 Braun, J., Burbidge, D., Gesto, F., Sandiford, M., Gleadow, A. J. W., Kohn, B.,
 1017 & Cummins, P. (2009). Constraints on the current rate of deformation and
 1018 surface uplift of the australian continent from a new seismic database and
 1019 low-t thermochronological data. *Australian Journal of Earth Sciences*, *56*(2),
 1020 99–110.
- 1021 Burstedde, C., Wilcox, L. C., & Ghattas, O. (2011). p4est: Scalable algorithms for
 1022 parallel adaptive mesh refinement on forests of octrees. *SIAM Journal on Sci-*
 1023 *entific Computing*, *33*(3), 1103–1133.
- 1024 Calais, E., & Stein, S. (2009). Time-variable deformation in the new madrid seismic
 1025 zone. *Science*, *323*(5920), 1442–1442.
- 1026 Capitanio, F. A., Morra, G., & Goes, S. (2009). Dynamics of plate bending at the
 1027 trench and slab-plate coupling. *Geochemistry, Geophysics, Geosystems*, *10*(4).
- 1028 Clevenger, T. C., & Heister, T. (2021, March). Comparison between algebraic and
 1029 matrix-free geometric multigrid for a Stokes problem on an adaptive mesh
 1030 with variable viscosity. *Numerical Linear Algebra with Applications*. doi:
 1031 10.1002/nla.2375
- 1032 Conrad, C. P., Bilek, S., & Lithgow-Bertelloni, C. (2004). Great earthquakes and
 1033 slab pull: interaction between seismic coupling and plate–slab coupling. *Earth*
 1034 *and Planetary Science Letters*, *218*(1-2), 109–122.

- 1035 Conrad, C. P., & Lithgow-Bertelloni, C. (2002). How mantle slabs drive plate tec-
1036 tonics. *Science*, *298*(5591), 207–209.
- 1037 Conrad, C. P., & Lithgow-Bertelloni, C. (2004). The temporal evolution of plate
1038 driving forces: Importance of “slab suction” versus “slab pull” during the
1039 cenozoic. *Journal of Geophysical Research: Solid Earth*, *109*(B10).
- 1040 Conrad, C. P., & Lithgow-Bertelloni, C. (2006). Influence of continental roots and
1041 asthenosphere on plate-mantle coupling. *Geophysical Research Letters*, *33*(5).
- 1042 DeMets, C., Gordon, R. G., Argus, D., & Stein, S. (1990). Current plate motions.
1043 *Geophysical journal international*, *101*(2), 425–478.
- 1044 Forsyth, D., & Uyeda, S. (1975). On the relative importance of the driving forces of
1045 plate motion. *Geophysical Journal International*, *43*(1), 163–200.
- 1046 Fraters, M. (2021, June). *The geodynamic world builder*. Zenodo. doi: 10.5281/
1047 zenodo.5014808
- 1048 Fraters, M., Thieulot, C., van den Berg, A., & Spakman, W. (2019). The geody-
1049 namic world builder: a solution for complex initial conditions in numerical
1050 modeling. *Solid Earth*, *10*(5), 1785–1807. doi: 10.5194/se-10-1785-2019
- 1051 Ghosh, A., Becker, T., & Humphreys, E. (2013). Dynamics of the north american
1052 continent. *Geophysical Journal International*, *194*(2), 651–669.
- 1053 Ghosh, A., & Holt, W. E. (2012). Plate motions and stresses from global dynamic
1054 models. *Science*, *335*(6070), 838–843.
- 1055 Gordon, R. G. (1998). The plate tectonic approximation: Plate nonrigidity, diffuse
1056 plate boundaries, and global plate reconstructions. *Annual Review of Earth
1057 and Planetary Sciences*, *26*(1), 615–642.
- 1058 Heister, T., Dannberg, J., Gassmüller, R., & Bangerth, W. (2017). High accuracy
1059 mantle convection simulation through modern numerical methods–ii: realistic
1060 models and problems. *Geophysical Journal International*, *210*(2), 833–851.
- 1061 Jarvis, G. T., & Mckenzie, D. P. (1980). Convection in a compressible fluid with in-
1062 finite prandtl number. *Journal of Fluid Mechanics*, *96*(3), 515–583.
- 1063 Kreemer, C., Blewitt, G., & Klein, E. C. (2014). A geodetic plate motion and global
1064 strain rate model. *Geochemistry, Geophysics, Geosystems*, *15*(10), 3849–3889.
- 1065 Kreemer, C., & Holt, W. E. (2001). A no-net-rotation model of present-day surface
1066 motions. *Geophysical Research Letters*, *28*(23), 4407–4410.
- 1067 Kronbichler, M., Heister, T., & Bangerth, W. (2012). High accuracy mantle convec-
1068 tion simulation through modern numerical methods. *Geophysical Journal In-
1069 ternational*, *191*, 12–29. doi: 10.1111/j.1365-246X.2012.05609.x
- 1070 Laske, G., Masters, G., Ma, Z., & Pasyanos, M. (2012). Crust1. 0: An updated
1071 global model of earth’s crust. *Geophys Res Abs*, *14*, 3743.
- 1072 Li, C., van der Hilst, R. D., Engdahl, E. R., & Burdick, S. (2008). A new global
1073 model for p wave speed variations in earth’s mantle. *Geochemistry, Geo-
1074 physics, Geosystems*, *9*(5).
- 1075 Liu, S., & King, S. D. (2019). A benchmark study of incompressible stokes flow in
1076 a 3-d spherical shell using aspect. *Geophysical Journal International*, *217*(1),
1077 650–667.
- 1078 Liu, S., & King, S. D. (2022). Dynamics of the north american plate: Large-scale
1079 driving mechanism from far-field slabs and the interpretation of shallow
1080 negative seismic anomalies. *Geochemistry, Geophysics, Geosystems*, *23*(3),
1081 e2021GC009808.
- 1082 Müller, R. D., Sdrolias, M., Gaina, C., & Roest, W. R. (2008). Age, spreading
1083 rates, and spreading asymmetry of the world’s ocean crust. *Geochemistry,
1084 Geophysics, Geosystems*, *9*(4).
- 1085 Nataf, H.-C., & Ricard, Y. (1996). 3smac: an a priori tomographic model of the up-
1086 per mantle based on geophysical modeling. *Physics of the Earth and Planetary
1087 Interiors*, *95*(1-2), 101–122.
- 1088 Osei Tutu, A., Sobolev, S. V., Steinberger, B., Popov, A. A., & Rogozhina, I. (2018).
1089 Evaluating the influence of plate boundary friction and mantle viscosity on

- 1090 plate velocities. *Geochemistry, Geophysics, Geosystems*, 19(3), 642–666.
- 1091 Osei Tutu, A., Steinberger, B., Sobolev, S. V., Rogozhina, I., & Popov, A. A. (2018).
 1092 Effects of upper mantle heterogeneities on the lithospheric stress field and
 1093 dynamic topography. *Solid Earth*, 9(3), 649–668.
- 1094 Pagani, M., Garcia-Pelaez, J., Gee, R., Johnson, K., Poggi, V., Styron, R., . . . Mon-
 1095 elli, D. (2018). Global earthquake model (gem) seismic hazard map (version
 1096 2018.1 - december 2018). *Creative Commons Attribution-NonCommercial-
 1097 ShareAlike 4.0 International License (CC BY-NC-SA)*.
- 1098 Priestley, K., McKenzie, D., & Ho, T. (2018). A lithosphere–asthenosphere bound-
 1099 ary—a global model derived from multimode surface-wave tomography and
 1100 petrology. *Lithospheric discontinuities*, 111–123.
- 1101 Ritsema, J., Deuss, A., Van Heijst, H., & Woodhouse, J. (2011). S40rts: a degree-
 1102 40 shear-velocity model for the mantle from new rayleigh wave dispersion,
 1103 teleseismic traveltimes and normal-mode splitting function measurements. *Geo-
 1104 physical Journal International*, 184(3), 1223–1236.
- 1105 Ritsema, J., & Van Heijst, H. J. (2000). Seismic imaging of structural heterogeneity
 1106 in earth’s mantle: evidence for large-scale mantle flow. *Science Progress (1933-
 1107)*, 243–259.
- 1108 Rolf, T., & Tackley, P. (2011). Focussing of stress by continents in 3d spherical man-
 1109 tle convection with self-consistent plate tectonics. *Geophysical Research Let-
 1110 ters*, 38(18).
- 1111 Saxena, A., Dannberg, J., & Gassmoeller, R. (2022, October). *Dataset for
 1112 High-resolution mantle flow models reveal importance of plate boundary
 1113 geometry and slab pull forces on generating tectonic plate motions.* Zen-
 1114 odo. Retrieved from <https://doi.org/10.5281/zenodo.7225629> doi:
 1115 10.5281/zenodo.7225629
- 1116 Schubert, G., Turcotte, D. L., & Olson, P. (2001). *Mantle convection in the earth
 1117 and planets*. Cambridge University Press.
- 1118 Simmons, N. A., Myers, S., Johannesson, G., Matzel, E., & Grand, S. (2015). Evi-
 1119 dence for long-lived subduction of an ancient tectonic plate beneath the south-
 1120 ern indian ocean. *Geophysical Research Letters*, 42(21), 9270–9278.
- 1121 Simmons, N. A., Myers, S. C., Johannesson, G., & Matzel, E. (2012). Llnl-g3dv3:
 1122 Global p wave tomography model for improved regional and teleseismic travel
 1123 time prediction. *Journal of Geophysical Research: Solid Earth*, 117(B10).
- 1124 Simmons, N. A., Schuberth, B. S., Myers, S. C., & Knapp, D. R. (2019). Resolution
 1125 and covariance of the llnl-g3d-jps global seismic tomography model: appli-
 1126 cations to travel time uncertainty and tomographic filtering of geodynamic
 1127 models. *Geophysical Journal International*, 217(3), 1543–1557.
- 1128 Stadler, G., Gurnis, M., Burstedde, C., Wilcox, L. C., Alisic, L., & Ghattas, O.
 1129 (2010). The dynamics of plate tectonics and mantle flow: From local to global
 1130 scales. *Science*, 329(5995), 1033–1038.
- 1131 Stanzione, D., West, J., Evans, R. T., Minyard, T., Ghattas, O., & Panda, D. K.
 1132 (2020). Frontera: The evolution of leadership computing at the national sci-
 1133 ence foundation. In *Practice and experience in advanced research computing*
 1134 (pp. 106–111).
- 1135 Steinberger, B. (2000). Slabs in the lower mantle—results of dynamic modelling
 1136 compared with tomographic images and the geoid. *Physics of the Earth and
 1137 Planetary Interiors*, 118(3-4), 241–257.
- 1138 Steinberger, B., & Calderwood, A. R. (2006). Models of large-scale viscous flow in
 1139 the earth’s mantle with constraints from mineral physics and surface observa-
 1140 tions. *Geophysical Journal International*, 167(3), 1461–1481.
- 1141 Styron, R., & Pagani, M. (2020). The gem global active faults database. *Earthquake
 1142 Spectra*, 36.
- 1143 Van Wijk, J. (2005). Role of weak zone orientation in continental lithosphere exten-
 1144 sion. *Geophysical Research Letters*, 32(2).

- 1145 Wu, B., Conrad, C. P., Heuret, A., Lithgow-Bertelloni, C., & Lallemand, S. (2008).
1146 Reconciling strong slab pull and weak plate bending: The plate motion con-
1147 straint on the strength of mantle slabs. *Earth and Planetary Science Letters*,
1148 *272*(1-2), 412–421.
- 1149 Zhong, S. (2001). Role of ocean-continent contrast and continental keels on plate
1150 motion, net rotation of lithosphere, and the geoid. *Journal of Geophysical Re-*
1151 *search: Solid Earth*, *106*(B1), 703–712.
- 1152 Zhong, S., Gurnis, M., & Moresi, L. (1998). Role of faults, nonlinear rheology, and
1153 viscosity structure in generating plates from instantaneous mantle flow models.
1154 *Journal of Geophysical Research: Solid Earth*, *103*(B7), 15255–15268.
- 1155 Zoback, M. D., Townend, J., & Grollmund, B. (2002). Steady-state failure equilib-
1156 rium and deformation of intraplate lithosphere. *International Geology Review*,
1157 *44*(5), 383–401.